1998

Characterization and Modeling of Advanced Modified Surfaces.

Vadim Gennadievich Palshin
Louisiana State University and Agricultural & Mechanical College

INFORMATION TO USERS

This manuscript has been reproduced from the microfilm master. UMI films the text directly from the original or copy submitted. Thus, some thesis and dissertation copies are in typewriter face, while others may be from any type of computer printer.

The quality of this reproduction is dependent upon the quality of the copy submitted. Broken or indistinct print, colored or poor quality illustrations and photographs, print bleedthrough, substandard margins, and improper alignment can adversely affect reproduction.

In the unlikely event that the author did not send UMI a complete manuscript and there are missing pages, these will be noted. Also, if unauthorized copyright material had to be removed, a note will indicate the deletion.

Oversize materials (e.g., maps, drawings, charts) are reproduced by sectioning the original, beginning at the upper left-hand corner and continuing from left to right in equal sections with small overlaps. Each original is also photographed in one exposure and is included in reduced form at the back of the book.

Photographs included in the original manuscript have been reproduced xerographically in this copy. Higher quality 6" x 9" black and white photographic prints are available for any photographs or illustrations appearing in this copy for an additional charge. Contact UMI directly to order.

UMI

A Bell & Howell Information Company
300 North Zeeb Road, Ann Arbor MI 48106-1346 USA
313/761-4700 800/521-0600

CHARACTERIZATION AND MODELING OF ADVANCED MODIFIED SURFACES

A Dissertation

Submitted to the Graduate Faculty of the
Louisiana State University and
Agricultural and Mechanical College
in partial fulfillment of the
requirements for the degree of
Doctor of Philosophy

in

The Interdepartmental Program
in
Engineering Science

by
Vadim G. Palshin
B.S., Moscow Institute of Physics and Technology, 1992
August, 1998

ACKNOWLEDGMENTS

The author would like to express his sincere appreciation to his major professor Dr. E.I. Meletis for his guidance and encouragement throughout this work. He would also like to thank Dr. T. Charalampopoulos, Dr. R. Kurtz, Dr. G.S. Lee, and Dr. G. Ding for valuable suggestions and participation in this research work as members of his examination committee.

He wishes to thank Dr. P. Schilling and Dr. R. Tittsworth for their advice and guidance during EXAFS measurements at the DCM beamline at LSU CAMD, and fruitful discussions.

He would like to acknowledge the LSU-Ukrainian Exchange Program and express his gratitude to its founder, Chancellor H. Rouse Caffey of LSU Agricultural Center, for moral and financial support and providing him with the opportunity to study at LSU.

The author also wishes to express his appreciation of support and encouragement he received from his family and friends.

TABLE OF CONTENTS

LIST OF TABLES

LIST OF FIGURES

ABSTRACT

A promising approach to surface modification involves diamondlike carbon (DLC) coatings with "functionally-graded surfaces" (FGS) as substrates. Titanium nitride substrates have a great potential as a FGS for the DLC coating, since titanium and titanium alloy surfaces processed by enhanced glow discharge nitriding develop a nitrogen concentration profile that results in gradual increase in the material hardness in the surface region.

An investigation of the atomic structure of DLC films and the surface layer structure produced in the enhanced glow discharge nitriding was conducted in the course of this work.

DLC and Si-DLC films were found to be mainly amorphous, dense and of high hardness, with featureless and very smooth surfaces. For the DLC films, the sp^3/sp^2 ratio varied between 3.2 and 4.1. A microstructure that can be described as small graphitelike clusters interconnected by a network of sp^3-bonded carbon was suggested for these films. Characterization of the Si-DLC films revealed a wide variation in the sp^3/sp^2 ratio, between 1.5 and 5.4. The effect of Si atoms incorporated in the DLC structure seems to be the prevention of aromatic clustering and promotion of the formation of sp^3 bonds. A structural model consisting of a mixed sp^2-sp^3 carbon network with the $C(sp^2)$ atoms present in olefinic rather than aromatic form was suggested.

X-ray absorption examination of the nitrided surfaces demonstrated an increase of the nearest-neighbor N coordination numbers and higher phase fractions of δ-TiN as the particle energy and current density were increased. Processing conditions corresponding to the energies of the bombarding particles around 1 keV resulted in relatively thick and continuous TiN layers with a structure virtually identical to that of the TiN standard.

A two-phase model of the outer layer, describing the structure as a mixture of δ-TiN and α-Ti, was proposed. This model was found to be in excellent agreement with experimental data for samples processed at the particle energies of approximately 1 keV and above.

The present results clearly show that the bombarding flux energy plays the key role in the formation of the outer layer structure and thus, the migration of nitrogen into the substrate.

CHAPTER 1

INTRODUCTION

Modern surface modification techniques represent one of the most important directions in development of advanced materials. Surface behavior of materials determines most of their properties and characteristics. Such surface-related problems as friction, wear, corrosion, fracture initiation and some others, can be successfully solved by creating advanced surfaces with unique properties. This approach also enables us to develop materials with beneficial "custom-built" surfaces without changing any desirable bulk properties (e.g. fracture toughness, rigidity, etc.).

The majority of surface modification methods can be assigned to one of two general classes based on the produced surface structure. The first class includes methods involving deposition of a thin film on the treated surface. These coatings can be produced by chemical vapor deposition (CVD), physical vapor deposition (PVD), sputter deposition, ion plating, and ion-beam-assisted deposition (IBAD). The second general approach is to modify in some way a thin layer of the original surface. This can be achieved by ion implantation and a variety of plasma-assisted methods.

The first class of surface modification methods includes deposition of various forms of hard amorphous carbon films, also known as diamond-like carbon (DLC). These coatings include pure amorphous carbon (a-C) films as well as carbon materials containing as much as 50 at. % hydrogen. Carbon materials containing hydrogen are sometimes called hydrogenated DLC (a-C:H). They are metastable and amorphous forms of carbon, and usually have both sp^2 and sp^3 bonds.

The tremendous recent technological interest in DLC films is caused by their excellent properties as coating materials, including high hardness, low friction and wear, and chemical inertness. But despite very intensive research efforts in the recent years, their precise atomic structure is not well understood.

Another group of surface modification techniques with a very high potential consists of plasma-assisted processes and belongs to the second category of surface modification methods. Plasma-assisted processes utilize the gas discharge phenomenon to produce energetic ions and neutrals at very low pressure, and can produce compound layers of desired thickness, followed by a diffusion zone, under the materials surface. This type of processing allows to clean a treated surface using sputtering by energetic inert gas ions and neutrals, resulting in very high quality of the produced surfaces.

Ion nitriding is one of such methods and is widely used as a surface modification technique for metals. In this process, the material serves as a cathode in a dc glow discharge of N_2. Conventional ion nitriding is conducted at high pressures (usually 1-10 Torr) and relatively low values of voltage, current density, and flux energy. Important processing parameters, such as pressure and cathode current density, are mutually dependent and can not be controlled separately, thus limiting the overall flexibility and control over the nitriding process. Numerous limitations of this process are eliminated in the Intensified Plasma-Assisted Processing (IPAP), a technique that has been recently developed in our laboratory. In addition, IPAP has been found to produce desirable high nitrides at the surface region and to significantly enhance nitrogen diffusion into the substrate.

To date, the exact nature of the nitriding mechanism and the structure of the nitrided outer layer as a function of the energetic particle bombardment in the enhanced glow discharge ion nitriding utilized in IPAP are not well characterized and understood.

Recently, advanced surface modifications have been developed that combine the aforementioned two treatments to create "functionally-graded surfaces" (FGS). In our laboratory, IPAP is first utilized in these combined treatments to create a graded nitrogen concentration profile that results in gradual increase in the material hardness in the surface region. Second, DLC is deposited on the nitrided surface that due to enhanced surface strengthening exhibits significant improvements in durability and performance. Today, these new advanced surface modifications with FGS are attracting an ever increasing interest.

Thus, the present work is aimed at developing a better fundamental understanding of the two major components involved in surface modification (structure of DLC and outer nitrided surface layer). It is expected that the present effort will allow to exploit the full potential of this type of treatment in a very wide range of engineering applications.

CHAPTER 2

OBJECTIVES

Although numerous beneficial properties of DLC films (high hardness, good chemical and wear resistance, etc.) are well known, a good understanding of the atomic structure of DLC has yet to be developed. For example, a structural model explaining the mechanisms of excellent wear resistance and low friction coefficient of DLC films is needed. Similarly, the structure of the outer nitrided layer developed during IPAP is of utmost importance and its role in the nature of the nitriding mechanism needs to be better understood.

More specifically, the objectives of this research are: (i) to study the characteristics of ion beam-deposited DLC and Si-DLC films and develop a structural model based of the characterization results; (ii) to study the effect of energetic particle bombardment during IPAP on the atomic structure and phase structure of the modified surface layers and to achieve a better understanding of the fundamental principles which govern the relationship between glow discharge intensification and characteristics of the surface layers produced during ion nitriding; (iii) based on the above, to improve our understanding of intensified plasma-assisted surface modification processing.

CHAPTER 3

BACKGROUND AND LITERATURE SURVEY

3.1 DLC Coatings

3.1.1 Synthesis and Processes

DLC films have been prepared by using a wide variety of deposition methods. The first diamond-like films were deposited by Aisenberg and Chabot [1] in 1971. In their device, carbon atoms were generated by sputtering carbon electrodes in an Ar plasma. Their films may have contained both a-C and diamond microcrystallites.

Since then, methods used to produce diamond and DLC films included various high temperature CVD techniques, based on the chemical decomposition of a carbon bearing gas phase on the growing film surface [2-4]. One of the widely used methods, known as plasma-assisted CVD (PACVD), utilizes deposition from an RF plasma sustained in hydrocarbon gases onto negatively biased substrates. Numerous ion beam-assisted deposition methods were also used to produce DLC coatings [1, 5, 6]. These methods are usually performed at lower temperatures, generally between 300-700 K, and include: (i) primary ion beam deposition of carbon ions with energies over 40-50 eV; (ii) deposition by sputtering a solid carbon source by ion beam, dc- and rf-plasma sputtering, dual beam method, carbon evaporation in combination with ion beam, etc.; (iii) ion beam plating of various hydrocarbons at acceleration voltages of 100-1000 V.

In carbon sputtering methods, carbon arrives at the substrate surface as neutral atoms and/or ions. In the plasma-assisted methods, the mixture of ions and neutrals is delivered to the surface using a bias voltage. In the dual beam deposition method,

carbon atoms are either sputtered from a graphite target or evaporated by a laser beam with simultaneous Ar^+ beam bombardment of the substrate surface. Hydrogen-containing a-C:H films can be produced by adding some hydrogen gas to the deposition atmosphere or to the ion source. The ion-beam methods allow to independently control the ion energy and the angle of incidence.

In methods using a hydrocarbon gas as the source of carbon (dc- and rf-plasma deposition and ionized hydrocarbon beam deposition), the substrate is bombarded with ionized hydrocarbon molecules, neutrals and ions of an inert gas (usually Ar^+), with energies typically below 1 keV. These methods usually result in higher hydrogen content of the films, which can be as high as 65 at.%. The hydrogen incorporated in the *a*-C:H films may play a very important role in the bonding configuration of the carbon atoms by helping to stabilize tetrahedral (sp^3) coordination, which is believed to be responsible for the diamondlike properties of the films. Therefore, the optical, electrical, and mechanical properties of the films are closely related to the hydrogen content of the films.

Most processes also include the exposure of the treated surface to bombardment by ions of medium energy (up to 500 eV) during deposition, which seems to promote sp^3 - bonding and has a positive effect on the films properties. The hydrogen content and its form in DLC films can also be affected by energetic particle bombardment. The C-C bond strength (607 kJ/mol) is greater than that of C-H bond (337.2 kJ/mol). With increasing ion energies, some of the hydrogen may be stripped off as a result of energetic impacts. The hydrogen remaining in the films may simply be buried in the free

state. The hydrogen present in DLC films may, therefore, exist in both bound and unbound forms.

3.1.2 Structure and Proposed Models

Carbon can exist as three main allotropes: diamond, graphite, and amorphous carbon. These three forms have very different structure and thus different properties. Diamond is a metastable phase of carbon at the room temperature and atmospheric pressure. Diamond has a cubic structure (fcc with 000, 1/4 1/4 1/4 basis) and an extremely high density (3.5 g cm^{-3}). Graphite has a hexagonal structure with sp^2-bonded two dimensional planes interconnected by weak forces, and its density is much less than that of diamond (2.6 g cm^{-3}).

A carbon atom can exhibit three different types of electron hybridization, sp^3, sp^2 and sp^1. In the sp^3 hybridization, found in diamond, each of the four valence electrons lies on a tetrahedrally oriented sp^3 orbital. Each sp^3 hybrid orbital makes a strong σ bond with an adjacent atom. The three-fold coordinated sp^2 hybridization is found in graphite. In this configuration, three valence electrons belong to trigonal sp^2 hybrid orbitals which produce strong σ bonds with adjacent atoms in this layer. The fourth electron is assigned to a p_π orbital which lies normal to that plane and forms weak π bonds with π orbitals of adjacent planes. In sp^1 configuration, as in acetylene, two valence electrons are in linearly oriented sp^1 orbitals which form σ bonds, and the other two belong to $p_{y\pi}$ and $p_{z\pi}$ orbitals.

The precise atomic structure of DLC films is not well understood. Depending on which deposition process is used in preparation of DLC films, it is possible for the

carbon atoms at the surface to form all possible combinations of sp^1, sp^2, and sp^3 bonds. Most known forms of disordered carbon, such as soots, carbon fibers, glassy carbon and evaporated amorphous carbon, are basically sp^2 - bonded. Some carbon atoms in DLC have chemical bonds similar to those in diamond (sp^3 - bonding), although without long-range order. In short range, however, DLC exhibits extensive sp^3 bonding which is thought to be responsible for the diamond-like properties of these films. In long range, DLC is believed to be predominantly amorphous consisting of small isolated sp^2 - bonded (graphitic) clusters captured in a partially hydrogenated random network of sp^3 coordinated carbon.

Recently, Tamor and Wu [7] suggested a graphitic network model for the atomic structure of DLC. Their defected graphite (DG) model is based on a structure which differs from graphite only in the random distribution of a single type of nonaromatic defect in sufficient density to induce strong π-electron localization. In a perfectly ordered, infinite graphite sheet, π-electrons are completely delocalized and behave as metal electrons. In a defected area where a carbon atom is absent or rehybridized, a region of low π-electron density is created. In a two dimensional case, a relatively small degree of such disorder will induce localization, which can be considered "weak" in the sense that the sheet remains conductive. A random distribution of such defects can leave only small clusters of closed sp^2 rings, or aromatic domains, connected by short chains. The bonding type in these chains will depend on the choice of the defect.

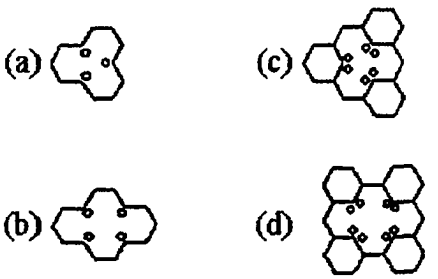

Figure 1 Schematic diagrams of the nonaromatic region for simple defects in a graphitic network. (a) A single vacancy with sp^2 coordination of the surrounding carbon, (b) nearest-neighbor pair vacancy with sp^2 coordination, (c) single vacancy with sp^3 coordination, and (d) nearest-neighbor pair vacancy with sp^3 coordination [7].

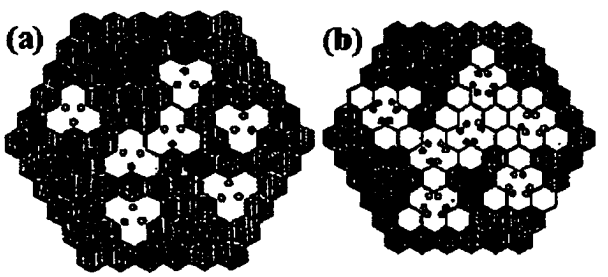

Figure 2 Diagram of a 91-ring graphitic cluster with 7 randomly removed carbon atoms. Each circle indicates a hydrogen atom [7].

The authors define "aromatic" region as hexagonal rings of sp^2-coordinated carbon, and a nonaromatic defect as a group of the rings made nonaromatic by a structural defect of the carbon network. Figure 1 shows nonaromatic defects created by single or paired vacancies. Hydrogen atoms are shown as open circles.

Figure 2 (a) demonstrates a 91-ring cluster with 7 carbon vacancies, where each carbon atom adjacent to a vacancy is bonded to only one hydrogen, and so remains sp^2 hybridized. Figure 2 (b) shows the same cluster, but with two hydrogen atoms bonded to each carbon atom surrounding the vacancy, with sp^3 coordination of these carbon atoms. Therefore, the DG model allows the sp^3-type bonds only when hydrogen atoms

are present, as in a-C:H, and predicts a linear increase in the sp^3/sp^2 ratio with increasing hydrogen content.

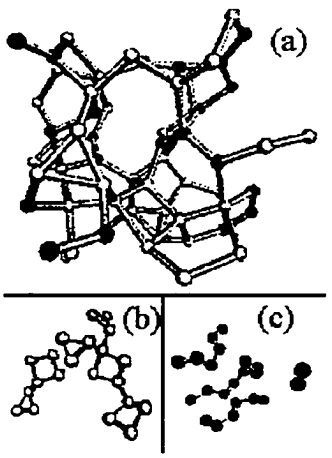

Figure 3 64 atom ta-C network, (a) the complete 64 atom structure, (b) the three- and four-membered rings, (c) the 22 sp^2 hybridized carbon atoms grouped into clusters [8].

Table 1 Comparison between structural characteristics of simulated ta-C and experimental data [8].

Quantity	Simulated network	Experiment
First nearest neighbor distance r_1 (Å)	1.52	1.52-1.53
Second nearest neighbor distance r_2 (Å)	2.50	2.50
First coordination number N_1	3.65	3.93
Second coordination number N_2	9.65	7.7-11.3
sp^3 fraction	0.65	0.80

Marks et al. [8] reported simulations of a highly tetrahedral amorphous carbon (ta-C) network with a density of 3 g cm^{-3}. The simulated network consists of 65% sp^3 and 35% sp^2 coordinated carbon atoms, which is in reasonably good agreement with experimental data. In this model, the ta-C is viewed as a random tetrahedral network with a "contamination" of sp^2 bonding. The resulting network has a significant amount of three-membered rings of sp^3 bonded atoms, similar to cyclopropane (C_3H_6), and four-membered rings as in cyclobutane (C_4H_8). This structure, consisting of 22 sp^2 and 42

sp^3 atoms, is shown in Fig. 3. Frequently occurring three-, four-, and five-membered rings give this network its distinct topology. The basic structural parameters of the ta-C network are summarized in Table 1.

Wang et al. [9] studied the structural properties of a-C with tight-binding molecular dynamics simulations. In the resulting amorphous carbon model, the threefold coordinated atoms form clusters embedded in the matrix of both twofold and fourfold atoms. These clusters are graphite-like sheets of about 10 Å×10 Å in size, containing mostly six- and some five- and seven-membered rings. The twofold and fourfold coordinated atoms serve mostly as bridges connecting the graphite-like clusters. As the network density was increased, the graphite-like clusters shrink in size, while the "bridge" areas expand and are increasingly dominated by fourfold atoms, which also tend to form clusters. Similar models describing graphite-like clusters in a random matrix of disordered twofold and fourfold coordinated atoms proposed by Comelli et al. [10], and by Robertson and O'Reilly[11], are discussed below.

The EXAFS study of DLC films reported by Comelly et al. [10] suggested that the film structure consists of graphite-like regions embedded in a random matrix of amorphous material. The random matrix is mainly composed of statically and dynamically disordered network, and the graphite-like regions consist of a network of odd- and even-membered conjugated rings. This study showed the need for a two-phase model of DLC structure, where both phases lack intermediate and long range order and can be considered amorphous.

Robertson and O'Reilly [11] studied the electronic structure of a-C and a-C:H through calculations on a number of model structures containing different possible configurations of sp^2 and sp^3 sites. They found that the most stable arrangement of sp^2 sites was in compact clusters of fused six-fold rings, or graphitic layers, with the width of the optical gap varying inversely with the sp^2 cluster size. These results suggested a model consisting of disordered graphitic layers of about 15 Å in diameter, bounded by sp^3 sites.

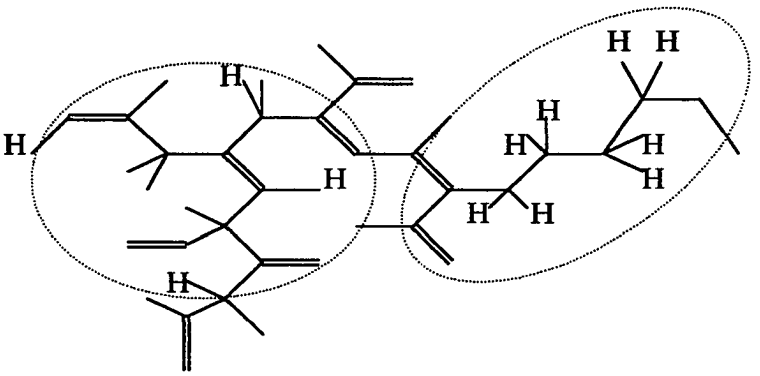

Figure 4 Schematic model of the microstructure of a-C:H, with $C(sp^2)$ present in olefinic rather than aromatic form [12].

Another model of DLC structure based on NMR investigations was proposed by Jager et al. [12]. In this model, shown in Figure 4, most of the sp^2 carbon is in the olefinic and not on the aromatic/graphitic form, and the DLC structure consists of short sections of CH_2 chains and statistically distributed CH groups in the sp^2-sp^3 carbon network, with the hydrogen predominantly bonded to $C(sp^3)$ atoms. These two environments are separated by regions of nonhydrogenated sp^2 carbon atoms. It has been concluded from these results that there are relatively few $C(sp^3)$-$C(sp^3)$ tetrahedral units contributing to the hardness of the alloys. Instead, bonded pairs of olefinic $C(sp^2)$ atoms are proposed to be responsible for the observed high hardness, and the hydrogen

is proposed to be more important as an inhibitor of aromatic clustering than as a means of increasing the fraction of sp^3 sites.

3.1.3 Characterization and Properties

DLC coatings have become a subject of a very intensive and widespread research due to their unique properties. They exhibit very high hardness, low friction and wear, chemical inertness and optical trasparency. This combination of properties allows the use of DLC in such applications as wear-resistant coatings for metals and ceramic materials, antireflective coatings for optical elements, corrosion protection, and many others.

The term DLC has been used to describe pure amorphous carbon (a-C) coatings as well as amorphous, hard carbon materials containing as much as 50 at.% hydrogen (a-C:H). Hydrogen atoms are usually introduced into the structure because hydrocarbon gases such as methane or acetylene are used to deposit DLC. The hydrogen atoms in DLC structure are thought to stabilize the sp^3 bonds [1]. Based on the structural models of DLC films described above, the principal requirement for modeling the structure of a-C or a-C:H is to find the fraction of sp^2 and sp^3 bonds and the hydrogen content.

Structure and properties of DLC films have been studied using various characterization techniques, some of which are summarized below.

Raman spectroscopy is based on the inelastic scattering of photons in the optical range of lattice vibrations. Raman spectra are sensitive to changes in translational symmetry and can be used to study disorder, formation of crystallites, or changes in structure in DLC films. Laser beams utilized in Raman spectroscopy can penetrate only

a thin layer of carbon (20-50 nm) and provide information on surface layer structure of DLC films.

The first order Raman spectrum of diamond is a single line at 1332 cm^{-1}, and that of graphite is a line at about 1580 cm^{-1} [13, 14]. In disordered graphite, which does not have the long-range translational symmetry, crystal momentum is no longer conserved, and this causes significant changes in the spectrum. The most pronounced effect is that in addition to G band, another disorder, or D, broad line appears at about 1355 cm^{-1}, which is also associated with in plane vibrations.

X-ray diffraction (XRD) measurements of DLC often demonstrate the presence of diamond crystallites with sizes from several to tens of nanometers, although isolated crystallites up to 5 μm in diameter have been reported [15]. Electron diffraction (ED) studies using transmission electron microscopy (TEM), sensitive on the scale of short interatomic distances, are more suitable for studying the short-range structure. In addition, TEM observations of thin DLC films can also provide important microstructural information. Very little work has been performed in this area and ED patterns of DLC films indicate wide diffuse diffraction rings, suggesting an overall amorphous nature of the films [16].

X-ray photoelectron spectroscopy (XPS) and Auger electron spectroscopy (AES) are very powerful techniques for surface composition analysis. Unless depth profiling measurements are required, these characterization techniques are non-destructive, and can provide valuable information on bonding between atoms and on core level binding energies. The chemical bonding information contained in XPS and

AES spectra can be used to distinguish both the element and its chemical state [17]. Both XPS and AES are very well suited for characterization of very thin films, such as DLC, due to the fact that ejected electrons escape only from the first few atomic layers of the surface.

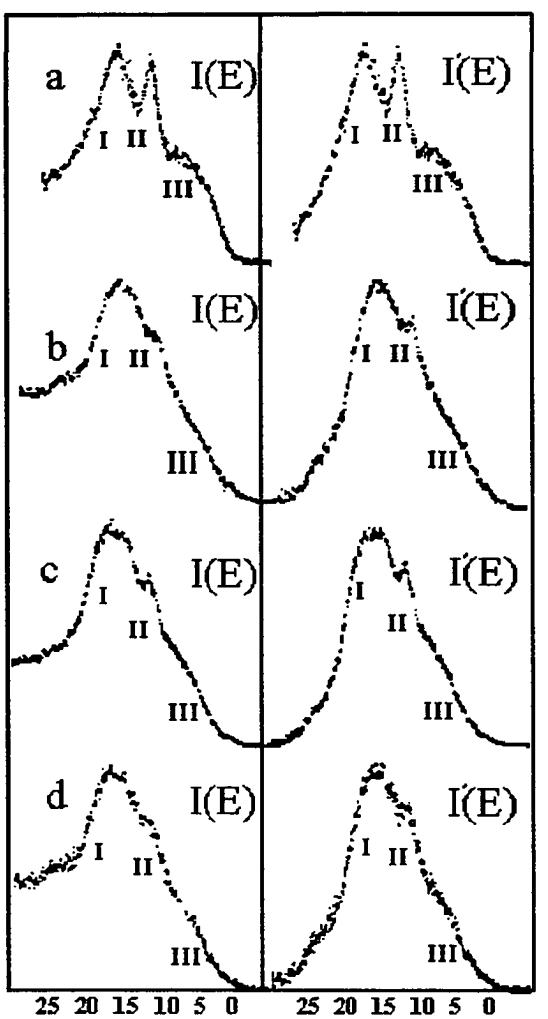

Figure 5 Valence-band XPS spectra of (a) diamond, (b) microcrystalline and (c) crystalline graphite, and (d) glassy carbon [18].

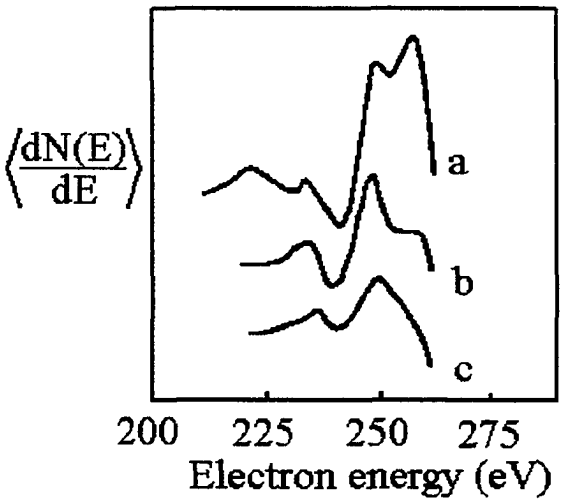

Figure 6 Fine structure of the carbon Auger spectra from (a) diamond, (b) graphite, and (c) amorphous carbon [1].

Because of the different coordination in graphite (trigonal) and in diamond (tetrahedral), there are substantial differences in their chemical bonding. High-resolution XPS spectra of diamond and graphite, presented in Figure 5, have three distinct spectral regions in the valence-bond spectra [18]. For diamond, region I has a peak between 16 and 21 eV binding energy (zero is the top of the valence band) and arises from *s*-like bands. Region II has a peak between 10 and 15 eV with a strong mixture of *s* and *p* character. Region III has a broad peak between 5 and 10 eV that is attributed to the *p* bands. For graphite, peak III can hardly be distinguished from the slope of peak II. The spectra of microcrystalline graphite and glassy carbon are similar to those of graphite.

In XPS, the electron energy distribution *N(E)* is usually used, while in AES the derivative *dN(E)/dE* of the electron energy distribution is used more frequently. Auger peaks are relatively sharp features on a slowly varying background, and they appear

more prominently on *dN/dE* spectra. Different carbon allotropes, that can be observed from the changes in the line shape of carbon Auger signals from diamond, graphite and amorphous carbon, are shown in Figure 6. The Auger signals for the DLC films lie somewhere between those of single-crystal graphite and natural diamond. The observable difference between DLC and graphite is that the shoulder in the DLC film spectrum at 250 eV is not as pronounced as that in the graphite spectrum. The spectrum for natural diamond shows no shoulder, and the main peak is shifted to higher energies, possibly due to the charging effect [19].

Infrared (IR) spectroscopy is often used to obtain quantitative information on the sp^1, sp^2, and sp^3 hybridization in a-C:H films from the C-H stretch in IR absorption spectra. A strong broad band at about 2900 cm^{-1} occurs due to C-H stretch vibrations, and curve fitting of this feature allows to differentiate between different kinds of electron hybridization [20, 21].

Thus, a wide variety of characterization techniques can be utilized to provide critical information needed to study the microstructural and structural aspects of DLC films.

3.2 Intensified Plasma Nitriding

3.2.1 Process Description

A number of limitations of ion beam implantation processes, such as their line-of-sight nature and the relatively shallow modified layer (typically below 0.5 μm), can be overcome in plasma ion nitriding where a glow discharge fully engulfs the substrate to ensure complete uniform surface treatment and creation of deeper layers.

Conventional ion nitriding utilizes a diode glow discharge process conducted at relatively high pressures, 1 to 10 Torr, and low bias voltages, 300-1000 V. The workpiece serves as cathode with a negative bias while the chamber is maintained at ground potential. High voltage is applied to the cathode in the presence of a gas and a glow discharge is produced, with the gas molecules ionized by colliding with electrons generated from the workpiece. The current density at the cathode is controlled by the gas pressure in the system. The diode system is usually operated in the abnormal glow discharge regime where the highest increase in current density as a function of bias voltage is observed. In order to sustain the plasma, diode systems have to be operated at high pressures, resulting in a low average ion and neutral energy. The diode plasma nitriding still has certain advantages compared to traditional nitriding processes which are carried out by using high temperature (1000°C or higher) gaseous media or liquid baths, namely relatively lower processing temperature, reduced processing time, energy savings and reduced environmental pollution.

Intensified Plasma-Assisted Processing (IPAP), is a technique recently developed in our laboratory [22-26]. IPAP employs a glow discharge in a triode configuration, as shown in Figure 7. This configuration allows to obtain highly energetic flux at relatively low pressures and temperatures compared to the conventional plasma nitriding, with the current density controlled independently of other process parameters such as bias voltage and pressure.

Glow discharge intensification is achieved by using a thermionic emission system. Electrons emitted from the filament are attracted by a positive electrode, gain

energy, collide with gas molecules in the plasma and ionize them. A small voltage (70-110 V) applied to the positive electrode allows to avoid electron accumulation in the vicinity of the filament. The ability to supply extra electrons into the plasma offers improved flexibility and greater control of the glow discharge. Independent control of such important process parameters as the cathode current density, cathode voltage and chamber pressure can provide numerous advantages over the conventional glow discharge processing [28, 29], including higher ionization efficiency, the ability to sustain plasma at low pressure and cathode voltage, increased particle energy, and reduced substrate temperature.

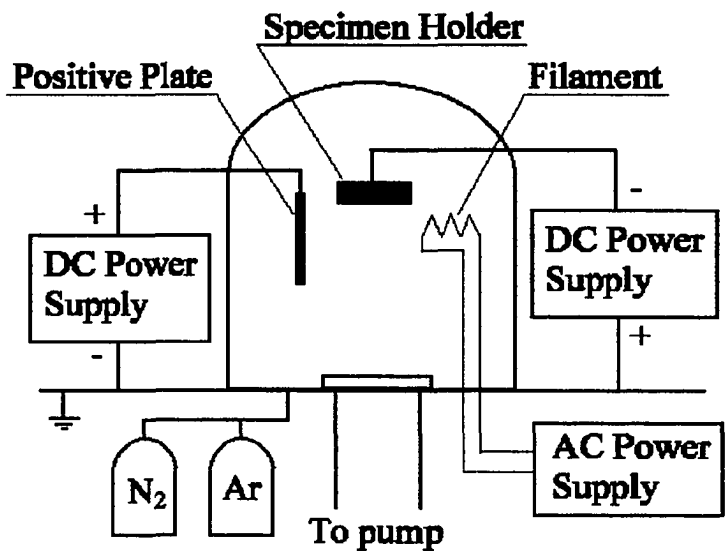

Figure 7 Schematic representation of enhanced glow discharge system [27].

Use of intensified plasma nitriding has allowed to process such difficult to nitride systems as austenitic stainless steel [23], pure Ti and Ti alloys [24] and aluminum [25]. AISI 304 stainless steel nitrided by IPAP revealed the presence of high nitrides, composed of a thin FeN layer followed by a thick layer of Fe_2N and Fe_3N. IPAP of

aluminum produced dense aluminum nitride with ultra-fine microstructure. Processing of pure Ti and Ti-6Al-4V alloy resulted in the formation of TiN and Ti_2N compounds followed by deep nitrogen diffusion zones. Nitriding of Ti alloys by conventional processing is very difficult, and it usually has to be done above the α/β transition temperature (~880°C). This high temperature process causes many undesirable effects, including differential expansion, residual stresses, and changes in microstructure. Also, it has been observed that during IPAP, nitrogen effective diffusivities increase dramatically (2-3 orders of magnitude) [23, 24]. These effects have been attributed to a higher extent of energetic particle bombardment during IPAP, although a clear understanding of these phenomena has yet to be developed.

In IPAP, the glow discharge operates in the abnormal regime, as shown in Figure 8. The space between the cathode and the anode can be divided into three regions: the ion sheath near the anode, the cathode dark space, and the negative glow. These three zones are schematically shown in Figure 9. The greatest potential drop occurs in the cathode dark space, and this is the most important area for ion nitriding. Secondary electrons produced at the cathode are accelerated across this region and gain energy for ionization and electron multiplication. The width of the cathode dark space L is approximately equal to the mean distance traveled by a secondary electron before its first ionization collision. In IPAP, the number of ionization collisions is increased by supplying additional electrons to the glow discharge.

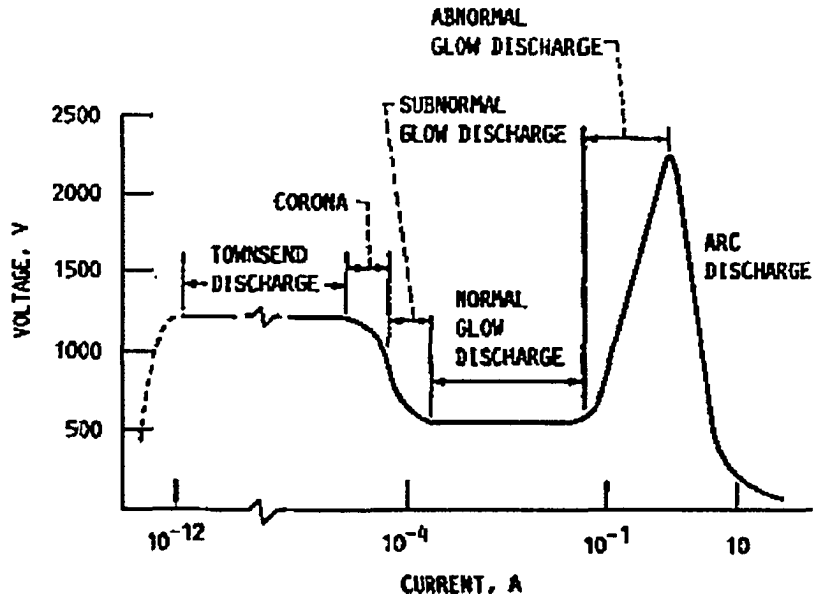

Figure 8 Glow discharge characteristic curve [30].

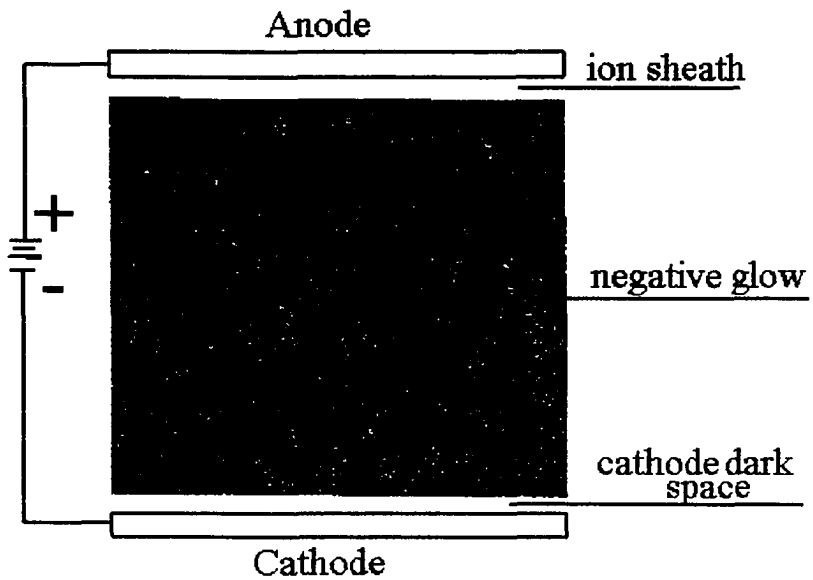

Figure 9 Schematic of the abnormal glow discharge [27].

It has been previously demonstrated in our laboratory [22] and by other researchers [31] that the equations developed in plasma physics for the dark space length and the ion energy distributions in the conventional glow discharge are applicable to enhanced glow discharge. The dark space length L is given by the Child-Langmuir equation [32, 33]:

$$L = \left(\frac{4\varepsilon_0}{9J}\right)^{1/2}\left(\frac{2q}{M}\right)^{1/4} V^{3/4}, \qquad (1)$$

where ε_o is the permittivity of free space ($8.85*10^{-12}$ F m^{-1}), J is the cathode current density, q is the ionic charge ($1.6*10^{-19}$ C), M is the ion mass ($M = 4.66*10^{-26}$ kg for N_2^+), and V is the bias cathode voltage ($V = V_C - V_p$, V_p being 10 V above the anode voltage). The mean free path for charge exchange collisions, λ can be found as:

$$\lambda = \frac{1}{\eta\sigma}, \qquad (2)$$

where η is the gas density (particles per cm^3) and σ is the collision cross-section ($2.5*10^{-15}$ cm^2 for the symmetrical charge transfer collision).

The collision mechanism in the dark space region of the glow discharge in shown schematically in Figure 10. Ions entering the dark space gain energy from the electric field. Some ions do not participate in any collisions and therefore do not lose energy, while other ions undergo collisions with neutrals on their way to the cathode.

The symmetrical charge exchange collision,

$$N_2^{+}{}_{FAST} + N_{2\,SLOW} \rightarrow N_2^{+}{}_{SLOW} + N_{2\,FAST},$$

produces a neutral with the energy equal to the ion energy before the collision and a new ion which starts accelerating and gaining energy from the field. Thus, ions and neutrals may have energies that vary from thermal (less than 1 eV) to that defined by the voltage applied to the discharge [22].

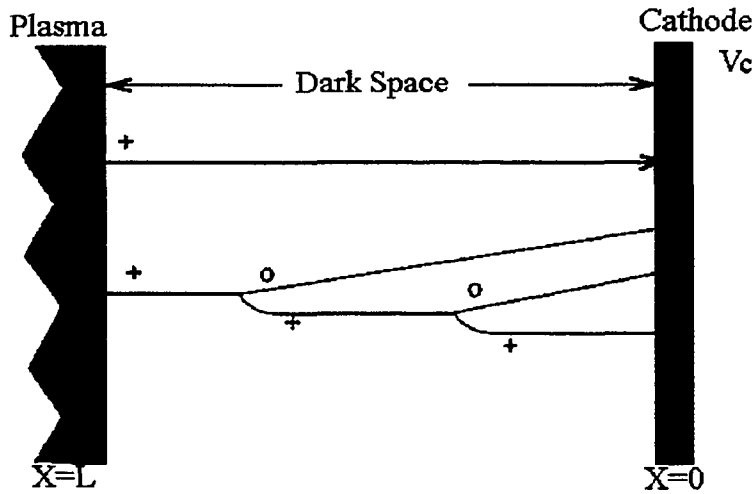

Figure 10 Mechanism of charge exchange collision in glow discharge [22].

The energy distribution of the ions arriving at the cathode is given by [34]:

$$\frac{dN}{dE} = \frac{N_i}{2}\frac{L}{\lambda}(1-E)^{-1/2}\exp\left[-\frac{L}{\lambda}+\frac{L}{\lambda}(1-E)^{1/2}\right], \qquad (3)$$

where N_i is the number of ions entering the dark space, and E is the ion energy normalized to the cathode voltage, V_C. This equation was derived by using the following basic assumptions: a charge exchange collision of an energetic ion and a neutral produces an equally energetic neutral and an ion with zero energy, the collision cross-section for charge transfer is independent of the ion energy, and the electric field decreases linearly from the cathode to the edge of the negative glow.

From the above equation, it can be shown that the energy of the ions that suffered collisions is:

$$E_i' = \int EN(E)dE = N_i V_C \left[2\left(\frac{\lambda}{L}\right) - 2\left(\frac{\lambda}{L}\right)^2 - e^{-\frac{L}{\lambda}} + 2\left(\frac{\lambda}{L}\right)^2 e^{-\frac{L}{\lambda}} \right]. \quad (4)$$

The number of ions that do not participate in collisions with neutrals and arrive at the cathode without any energy loss is:

$$N_f = N_i e^{-\frac{L}{\lambda}}. \quad (5)$$

The total energy of these ions is:

$$E'' = V_C N_i e^{-\frac{L}{\lambda}}. \quad (6)$$

Thus the total ion energy (E_i^t) is:

$$E_i^t = E_i' + E_i'' = N_i V_C \left[2\left(\frac{\lambda}{L}\right) - 2\left(\frac{\lambda}{L}\right)^2 + 2\left(\frac{\lambda}{L}\right)^2 e^{-\frac{L}{\lambda}} \right]. \quad (7)$$

The average ion energy E_i^a in the plasma can be calculated as [22]:

$$E_i^a = V_c \left[2\left(\frac{\lambda}{L}\right) - 2\left(\frac{\lambda}{L}\right)^2 + 2\left(\frac{\lambda}{L}\right)^2 e^{-L/\lambda} \right]. \quad (8)$$

Since the energy lost by ions during collisions is equal to the energy gained by neutrals, the number of energetic neutrals is equal to the number of collisions in the dark space:

$$N_n = N_i \frac{L}{\lambda}. \tag{9}$$

Therefore, the average energy of energetic neutrals can be expressed as [22]:

$$E_n^a = \frac{E_n^t}{N_i \frac{L}{\lambda}} = V_c \frac{\lambda}{L}\left[1 - 2\left(\frac{\lambda}{L}\right) + 2\left(\frac{\lambda}{L}\right)^2 - 2\left(\frac{\lambda}{L}\right)^2 e^{-\frac{L}{\lambda}}\right]. \tag{10}$$

The above equations demonstrate that the ratio L/λ is a critical parameter in energy distributions of ions and neutrals. Figures 11 and 12 show the effect of L/λ ratio on average and total particle energies. The average energies of both ions and neutrals decrease with increasing L/λ values. At low operating pressures achieved in IPAP the mean free path λ increases, and the number of charge exchange collisions is reduced. This results in low L/λ ratios and higher average ion energies.

While both average and total ion energy decrease with increasing L/λ, the number of the charge exchange collisions will grow. This leads to a greater increase in the number of energetic neutrals produced by the collisions compared to the increase in the total neutral energy, and the average neutral energy is decreased.

Previous research conducted in our laboratory [22] has demonstrated the existence of an optimal value for the L/λ ratio (~2) which maximizes the effect of the energetic particle bombardment. This can probably be attributed to the optimal balance between the two competing parameters, the number of energetic neutrals and the average neutral energy.

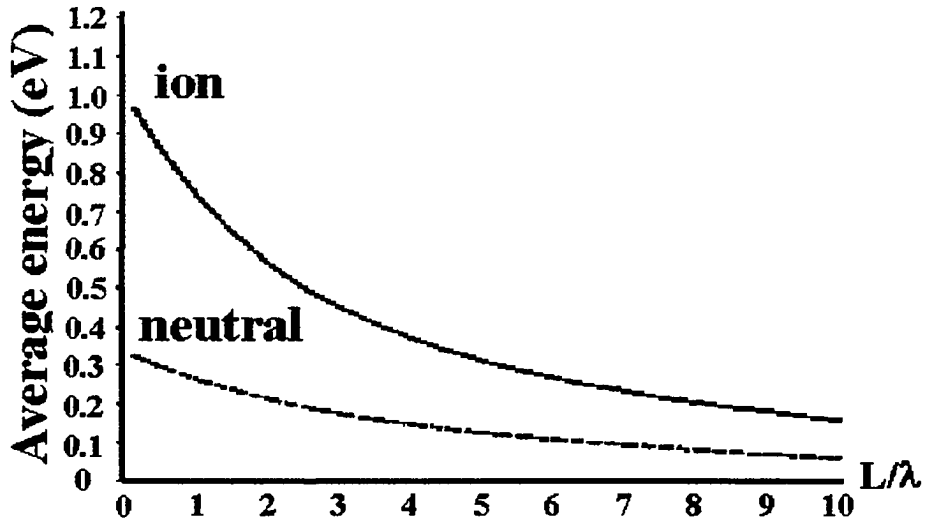

Figure 11 The relationship between average ion and neutral energies and L/λ [22].

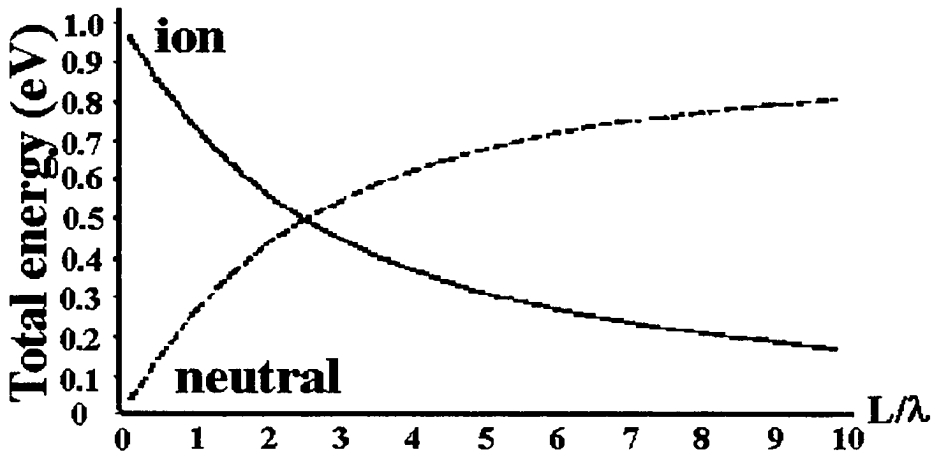

Figure 12 The relationship between total ion and neutral energies and L/λ [22].

3.2.2 Plasma Nitriding Mechanism

Plasma nitriding has long been available as an alternative to more conventional nitriding methods, and it is well established as an industrial process. Many aspects of plasma nitriding mechanism, however, are still not well understood. Previous studies have dealt with many metallurgical issues, but there is still a significant amount of contradiction concerning the nature of the active plasma particles responsible for the nitriding process. Seybolt [35] suggested thermal diffusion mechanism for ion nitriding, with neutral nitrogen atoms as the active plasma species. The nitriding process was explained by absorption of neutral nitrogen atoms at the substrate surface and their subsequent diffusion into the subsurface layers. Later, in a work reported by Tibbetts [36], nitriding effects of different particles were studied using a dc glow discharge over iron and steel surfaces, which could be biased to repel all positive ions. Experiments were conducted both with and without a grid that repelled cations. It was reported that neutral atomic nitrogen was capable of causing effective nitriding. Other authors [37,38] reported studies of chemical reactions between nitrogen and surfaces of silicon and silicon oxide by *in-situ* examinations that included X-ray and UV photoelectron spectroscopy, AES, secondary ion mass spectroscopy, and other characterization techniques. These researchers reported that N_2^+ ions undergo charge exchange and dissociation processes at very short (~5-6 Å) distances from the surface of the substrate, and strike the surface as neutral nitrogen atoms. The authors reported that the effect of ion kinetic energy in the reaction is negligible. In another work [39] supporting the theory of nitriding by active nitrogen atoms, collision dissociation mechanism was

proposed. In this model, energetic ions collide with nitrogen molecules which dissociate and produce active N atoms that form the nitride layer.

An alternative view supported by other researchers is that nitrogen ions are the species responsible for the nitride formation. In his study of the mechanism of ion nitriding in steels, Hudis [40] reported that gas absorption process was not responsible for nitriding. The surface hardness, which is related to the nitrogen content, was found to increase with increasing current density. The author concluded that plasma nitriding was caused by ionic bombardment of the cathode, and that nitrogen ions were the active plasma ingredient. It has been previously suggested [41] that surface layer subjected to energetic particle bombardment acts as a source of vacancies and interstitials. A model developed by Jones and Martin [42] also suggested that surface defects created by ion bombardment enhance diffusion of nitrogen. Brokman and Tuler [43] showed that the local effective nitrogen diffusivity is proportional to the cathode current density. They proposed that radiation damage produced by ion bombardment promotes the diffusion due to creation of such defects as vacancies, and formation of vacancy-ion pairs. The vacancy-ion pairs then migrate into the bulk by vacancy substitutional mechanism, with local effective diffusion coefficient higher than that for interstitial nitrogen diffusion.

It is evident from the above studies that the energetic particle bombardment is one of the most important factors affecting the structure of the outer layer formed during nitriding. When the energetic particles (ions or neutrals) penetrate the near-surface layer, atoms in the layer can be transported by collisions. They can obtain sufficient kinetic energy to be displaced away from their lattice sites, forming defects. Enhanced diffusion occurs as a result of defect production. These energy exchange

processes can generate nonthermal equilibrium states and form metastable phases at room temperatures.

Sputtering occurs continuously during plasma surface modification processes. When energetic particles strike a substrate, momentum transferred to substrate atoms leads to various interactions depending upon the energy of the particles. For a collision cascade close to the external surface, sufficient energy may be transferred to one or more atoms to be dislodged or sputtered from the surface. The penetration by energetic particles produces a collision cascade causing large numbers of atoms to be displaced, producing numerous interstitials and vacancies. These processes have been extensively studied in the past for high energy ion implantation processes, in the energy range of 10-100 keV. Relatively low energy particles encountered in plasma processes can also produce defects to a depth of several atomic layers from the surface. However, very little study has been previously conducted to investigate the sputtering process in this energy regime.

In a recent study by Adjaottor [44], sputtering and ion implantation effects caused by energetic particle bombardment of TiN substrates were investigated, using theoretical predictions produced by the TRIM program [45] as well as experimental measurements. It has been observed that experimentally determined sputtering yield curves demonstrated three regimes as a function of the average particle energy. Regimes I and III, below 200 eV and above 600 eV, respectively, showed reasonably good agreement with theoretical predictions. Regime II, in the 200-600 eV energy range, demonstrated substantially reduced sputtering rates that were seemingly independent of particle energy. Therefore, it has been suggested that at particle

energies above 200 eV subsurface effects such as defect generation start to become significant compared to sputtering effects. These observations seem to confirm that under certain plasma conditions, e.g. for particle energies above some threshold value, the energy of bombarding particles contributes to more beneficial effects such as subsurface defect formation.

Evidently, the role of bombarding particle energy in the plasma nitriding process and its effect on the resulting structure needs to be further investigated, and thorough structural studies are needed in this area to provide this critical information.

3.2.3 Characterization of Produced TiN Layers using EXAFS

3.2.3.1 Fundamentals of EXAFS

In this work, extended X-ray absorption fine structure (EXAFS) was used to characterize the local structure in the titanium nitride layers. EXAFS signal is the oscillatory variation in X-ray absorption as a function of photon energy just above an absorption edge. EXAFS spectra generally refer to the region 40-1000 eV above the absorption edge. Near or below the edge is the X-ray Absorption Near Edge Structure (XANES), where absorption peaks generally appear due to excitation of core electrons to some bound states (1s to nd, (n+1)s, or (n+1)p orbitals for K edge). This region contains valuable bonding information such as the energies of virtual orbitals, the electronic configuration, and the site symmetry.

The EXAFS structure may extend as far as 1 keV beyond the edge, with an amplitude typically 1-20% of the edge jump. It results from interference effects caused by scattering of the outgoing photoelectron from neighboring atoms. Figure 13 [46] schematically shows the radial portion of the photoelectron wave. The solid lines

indicate the outgoing wave of an isolated atom, and the dashed lines represent backscattering of the outgoing waves by neighboring atoms. Superposition of outgoing and scattered waves produces oscillatory behavior of absorption coefficient μ as a function of energy E. In a monatomic gas, such as Kr, a photoelectron ejected by absorption of an X-ray photon will travel as a spherical wave with a wavelength

$$\lambda = 2\pi/k, \qquad k = \sqrt{\frac{2m}{\hbar^2}}(E - E_0), \tag{11}$$

where E is the incident photon energy and E_0 is the threshold energy of the absorption edge, and EXAFS is absent.

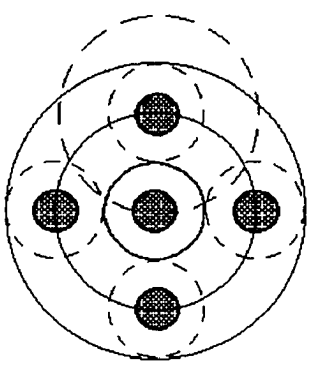

Figure 13 Schematic of the radial portion of the photoelectron wave [46].

EXAFS function χ is obtained by background removal and normalization of the absorption spectrum. Single scattering is extremely important in EXAFS, and the EXAFS formula in the single-electron single-scattering case is [47]

$$\chi(k) = \sum_j N_j S_i(k) F_j(k) e^{-2\sigma_j^2 k^2} e^{-2r_j/\lambda_j(k)} \frac{\sin(2kr_j + \phi_{ij}(k))}{kr_j^2} \tag{12}$$

where $F_j(k)$ is the backscattering amplitude from each of the N_j neighboring atoms of the j^{th} type, σ_j is Debye-Waller factor responsible for thermal vibration and static

disorder at a distance r_j away, ϕ_{ij} is the total phase shift experienced by the photoelectron, λ_j the electron free path, and $S_i(k)$ the amplitude reduction factor at central atom i due to many-body effects such as shake up/off process at the central atom. The term $e^{-2r_j/\lambda_j(k)}$ appears due to inelastic losses in the scattering process.

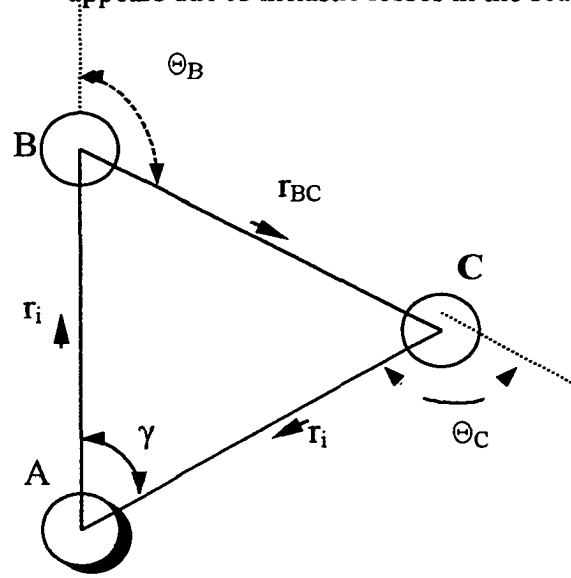

Figure 14 Illustration of a double scattering path.

Multiple scattering contributions are illustrated in Figure 14 for a three atom system, where atom A is excited by absorbing an X-ray photon.

EXAFS measurements can be performed by using several detection methods depending on the type of the specimen. The most common is the transmission mode, where the intensities before and after the sample are measured and converted to absorption according to the formula

$$\mu x = \ln(\frac{I_0}{I}), \qquad (13)$$

where μ is the linear absorption coefficient, x is the sample thickness, and I_0 and I are the intensities before and after the sample, respectively. This technique is simple and it

makes use of all incident photons, but may suffer from the thickness effect which sometimes can make the extraction of accurate amplitude information difficult.

EXAFS spectra can also be measured in the fluorescence mode. Fluorescence radiation is produced by filling of the core hole created by an X-ray photon. Since the background consists of scattered radiation (by elastic and Compton scattering) with energy higher than that of fluorescent radiation, the signal can be easily separated from the background. This makes the fluorescence mode preferable when the element of interest provides only a few percent of total absorption. Thickness effect is insignificant in this mode.

The third technique available for EXAFS measurements is the total electron yield (TEY) mode. The signal in TEY mode comes from Auger and photoelectrons produced by incident radiation, secondary electrons, and electrons produced by fluorescent radiation. Due to very small escape depth for electrons, only a thin (tens of nanometers) surface layer contributes to the signal. Since the thickness of this layer is much smaller than the absorption length, TEY signal is not affected by thickness or self-absorption effects. Thus, it is evident that TEY is an excellent technique to study the structure of the outermost nitrided layer.

3.2.3.2 Data Analysis

Data reduction is the first part in the EXAFS data analysis, and it consists of deglitching, energy alignment, background removal, normalization, and transformation to k space. After that, the structural parameters such as coordination numbers and bond lengths can be extracted by using Fourier transform of the data and nonlinear least-squares fitting technique.

The first step in data reduction is to convert the raw data into absorption coefficient vs. photon energy spectrum according to the equation

$$\mu(E)x = \ln(\frac{I_0}{I}) \tag{14}$$

for transmission,

$$\mu(E)x = F/I_0 \tag{15}$$

for fluorescence, and

$$\mu(E)x = I_{TEY}/I_0 \tag{16}$$

for the total electron yield mode. In these equations, I_0 is the incident intensity, and I, F, and I_{TEY} are the measured signal intensities for the free different detection modes.

Sharp "glitches" that may sometimes appear in the experimental spectra should be removed before any further processing of the data is performed. These features are not part of the actual data in the sense that they are caused by spurious reflections from the monochromator crystal, rather than by X-ray absorption by the sample. If left in the spectrum, these features may adversely affect the background removal process and reduce the result accuracy. Deglitching of the data can be accomplished by polynomial interpolation of the data points between the sides of the glitch, or simply by deleting the data in that region.

The EXAFS signal $\chi(E)$ is obtained according to equation

$$\chi(E) = \frac{\mu(E) - \mu_0(E)}{\mu_0(E)}, \tag{17}$$

where $\mu_0(E)$ is the absorption coefficient of an isolated atom. After the background $\mu(E) - \mu_0(E)$ is removed and the data is normalized with respect to $\mu_0(E)$, the EXAFS

signal in k space, $\chi(k)$, is obtained by converting the energy E into the photoelectron wavevector k according to the equation (11).

Fourier transform (FT) of the EXAFS signal is used to isolate the part of the data that corresponds to the nearest coordination shells and can be used to obtain quantitative information about the local environment. The radial distribution function produced by the Fourier transform of $\chi(k)$ allows to isolate the single shell data. It is accomplished by performing inverse FT of the transformed data over the data range that corresponds to that shell in r space. A common approach to the analysis of the single-shell data as well as the data from more than one shell is the use of numerical fitting techniques. The experimental spectrum $\chi(k)$ is fitted with the EXAFS equation

$$\chi(k)=S_0^2\sum_j N_j F_j(k) k_j^{n-1} e^{-2\sigma_j^2 k_j^2} e^{-2r_j/\lambda_j(k_j)} \frac{\sin(2k_j r_j+\phi_j(k_j))}{r_j^2}, \qquad (18)$$

where S_0^2 is the amplitude reduction factor, N_j and r_j are coordination number and bond distance, σ_j the mean square deviation from the bond distance, and λ_j the inelastic electron mean free path. The form of this equation requires the use of nonlinear fitting algorithms even in single-shell data analysis.

CHAPTER 4

EXPERIMENTAL PROCEDURES

4.1 Deposition of DLC and Si DLC Films

Diamond-like carbon films were deposited on Ti-6Al-4V alloy, M 50 steel and pure Si single crystals by ion-beam deposition. The deposition process was conducted in three steps. The first step was sputter cleaning of the substrate for approximately 3 minutes by 1 keV Ar^+ beam. Then, a 500 Å thick Si bond layer was deposited by either e-beam evaporation or ion-beam assisted deposition (IBAD), with substrate surface bombarded by 1 keV Ar^+ beam during Si vapor deposition. Finally, methane was fed into a Kaufman-type gun and DLC deposition was conducted for 4 hours at room temperature using an acceleration energy of 750 eV and a current density of about 2.5 mA cm^{-2}.

It was determined that in the presence of the Si interlayer the structure of the DLC films was independent of the nature of the original substrate material. The DLC films with the two different Si deposited interlayers are designated as Film 1 (e-beam Si deposition) and Film 2 (IBAD of Si). Thin DLC films of about 500 Å were also deposited on cleaved NaCl single crystals (with a 20 Å Si interlayer) and were used for TEM examinations.

Deposition of Si-DLC films on Si substrates was performed using energetic Ar^+ ion beam bombardment of a vapor-deposited precursor material: tetraphenyl-tetramethil-trisiloxane (704 Dow-Corning diffusion pump oil) [48-50], with the

precursor heated to 125 °C. A Zymet 100 non mass analyzed ion implanter was used first for sputter-cleaning of the substrate with a 40 keV Ar^+ beam and subsequently for the ion bombardment of the precursor material. Two groups of Si-DLC films were deposited, with the growing film surface bombarded with 50 keV Ar^+ beam in the first group (Films 1-3), and with 40 keV beam in the second (Films 4 and 5). Films were deposited at varying current densities, ranging from 85 μA cm^{-2} (Film 1) to 195 μA cm^{-2} (Film 5).

4.2 Characterization of DLC Films

The developed DLC films were characterized by the following techniques: Scanning electron microscopy (SEM), AES, TEM, IR spectroscopy, and Raman spectroscopy. Surface microhardness measurements were taken from the as-deposited Si-DLC films using a Knoop indenter and surface characteristics were obtained using surface profilometry. SEM studies of fractured film cross sections was used to determine film thickness and study film morphology and adherence to the substrate. Fourier transform infrared (FTIR) spectroscopy was conducted to obtain bonding characteristics and determine sp^3/sp^2 ratios. FTIR was performed by using a Perkin Elmer spectrometer that was scanned from about 400 cm^{-1} to 4000 cm^{-1}. An Auger/XPS Perkin Elmer spectrometer was used for AES analysis. AES was conducted at a 3 keV, 40 μA primary electron beam and a modulation voltage of 6 eV. TEM was performed on thin DLC films that were deposited on NaCl cleaved crystals. The NaCl substrates were dissolved in water and the films were transferred onto a copper grid for examination. Bright and dark field imaging was used for observing the film

microstructure and electron diffraction was used to obtain structural information. Raman spectroscopy was performed by near backscattering geometry using an Ar^+ laser operated at 514.5 nm (2.41 eV) at a power of 30 mW. Raman spectra were detected with a Ramalog 5 double spectrometer of SPEX, scanned from 900 cm^{-1} to 1800 cm^{-1}. After a linear background was subtracted, the spectra were deconvoluted using two Gauss functions.

4.3 IPAP Processing System

A new surface modification system designed and constructed in our laboratory allows three modes of operation, namely plasma treatments, ion beam treatments and sputter deposition. A schematic representation of the system is shown in Figure 7. The unit consists of a base plate connected to the mechanical and diffusion pumps, a cylindrical stainless steel chamber and a top plate supporting the specimen holder. All three system components have ports to accommodate electrical and mechanical feedthroughs.

A 3 cm filamentless broad beam ion source by Anatech Ltd. is attached to the bottom plate and is connected to electrical and gas feedthroughs through the bottom plate ports. The ion source is powered by Anatech's model IS-3000 power supply and is capable of delivering energetic particles in the energy range of 5 eV to 1200 eV. The ion gun is mounted on a swivel collar mount allowing height, tilt and rotational motion.

A Torus 2 d.c. magnetron sputtering source with a 5 cm diameter target is also attached to the bottom plate. It is powered by the MDX 500 magnetron drive and has a sputtering power of 1 kW. The growth rate and thickness of depositing thin films are monitored by a Leybold Inficon IPN-750-211-G1 thin film sensor. The sensor is

installed close to the specimen in-line view from the magnetron and ion beam source and regulated by an LH Inficon deposition monitor (model XTM/2) which displays the deposition rate, thickness and elapsed time.

The plasma intensification system is composed of a thermionic emission filament and a positive electrode. A 0.05 cm diameter tungsten wire is used as the thermionic filament (from R.D. Mathis company). A stainless steel plate (8 cm*6 cm) is used as the positive electrode and is positioned diametrically opposite from the filament. The positive plate is operated by a 250 W low current HCR power supply (model 150-2-110).

A new high voltage cathode assembly is capable of providing rotational motion to ensure uniform processing conditions (nitriding or film deposition). The cathode is powered by a Hewlett Packard 6522A high voltage, low current power supply. Also, an eccentric hole is drilled in the high voltage rod up to its bottom threaded end allowing a chromel-alumel thermocouple to be inserted and record temperature during processing. The thermocouple is imbedded in a thin alumina tube ensuring electrical insulation from the high voltage rod.

Various gases can be introduced into the chamber. Gas flow is controlled by two MKS mass-flow controllers (Type 1159) and monitored by an MKS Type 247C 4-channel readout that can also control ratios of gases admitted in the chamber. Vacuum level in the chamber is monitored by an MKS baratron Type 122A absolute pressure gauge powered by an MKS Type PDR-D-1 power supply with digital readout. In the lower region of the unit below the base plate, there are two thermocouple vacuum

gauges to monitor pressure in the foreline to the diffusion pump and the bottom of the chamber. Vacuum in this system is maintained by a Varian NHS4 diffusion pump filled with DOW Corning 704 pump fluid and an Alcatel 2030 mechanical pump capable of pumping 765 l min^{-1}.

4.4 Preparation of TiN Specimens

Prior to surface treatment the specimens were ultrasonically cleaned in methanol and dried in air. Following polishing and cleaning, specimens were secured onto the specimen holder and then attached to the cathode rod. A standard procedure of elimination of contaminants in the chamber and on the specimen followed, where the chamber was initially pumped down with the mechanical pump to about 0.1 Torr and then the diffusion pump was used to obtain a vacuum level of about $1*10^{-5}$ Torr. The chamber was backfilled with Ar (99.99%) to 0.1 Torr and then pumped down again to $1*10^{-5}$ Torr. This flushing process was performed to expel residual air (oxygen) and other gas contaminants. A glow discharge was visible as a uniform purple color plasma around the cathode during sputter cleaning. After sputter cleaning the argon was gradually replaced with nitrogen and the desired operating pressure was maintained. Subsequently, the selected cathode voltage was applied and the positive electrode was biased at a positive potential in the range of 70 - 90 V. The purpose of the positive electrode is to attract and accelerate electrons generated by the filament. The specimen was then processed for the selected period of time. At the completion of the run, the filament was slowly turned off followed by the power to the positive electrode and finally cathode voltage. The nitrogen was replaced again with Ar, the high vacuum

valve was closed, and the specimen was allowed to cool slowly in the chamber to room temperature in the Ar atmosphere.

4.5 TiN Surface Analysis

XAFS spectra at the K edge of titanium (4966 eV) were recorded at the Center for Advanced Microstructures and Devices (CAMD), Louisiana State University. Data were collected using bending magnet radiation at the DCM1 beamline [51], where the X-ray beam was monochromatized with a fixed exit double crystal monochromator operating with Si(220) crystals. The incident monochromatic X-ray intensity before the sample (I_0) was monitored with an ionization chamber filled with one atomosphere of air and XAFS spectra were recorded in total electron yield (TEY) mode, with one atmosphere of helium in the detector chamber. EXAFS spectra were recorded over an energy range of 4800 – 5970 eV with 1 eV steps; XANES spectra were recorded from 4910 – 5400 eV with 0.2 eV steps in the near edge region.

Concentration profiles of chemical elements present in the nitrided layer and specifics of fracture properties of the samples were studied using a JAMP-10 S (JEOL-JAPAN) Auger spectrometer. The spectrometer was modified to allow fracturing of specimens in vacuum. Fracture surfaces were then studied with electron microscopy to provide specifics of the fracture properties of the samples. Fracturing the samples in the working chamber at very low pressures ($5\text{-}6*10^{-8}$ Pa) provides a "clean" surface, without adsorbed atoms and molecules of O, C, N, etc. The e-beam scanning system and appropriate detectors used with the system allow surface imaging with characteristic and secondary electrons with 250 Å resolution. In the Auger-electron

microscopy mode, the characterized area is below 1 μm in diameter at primary beam current 10^{-6}-10^{-7} A and bias voltage 10 kV.

Sputtering of the characterized surfaces with an ion gun was used for layer-by layer analysis of the samples. An Ar^{+} ion beam with an energy of 3 keV was focused on the specimen to produce a spot size of about 2 mm for sputtering.

Crystal structures and lattice parameters of the produced nitrides were studied by XRD to complement the EXAFS analysis. Diffraction patterns were obtained from the near-surface region (low angle) of the films using filtered Cu - K_{α} radiation (λ=1.542 Å).

CHAPTER 5

RESULTS AND DISCUSSION

5.1 Investigation of Ion Beam Deposited DLC Film structure

5.1.1 Characterization of DLC Films

Diamond-like carbon films with essentially featureless and very smooth surfaces (mean surface roughness less than 0.03 μm) were produced under the present IBD conditions, with a thickness of approximately 0.4 μm (as measured by SEM). The microhardness of the films (Knoop at 25g) was found to vary from about 2900 kg mm^{-2} for Film 1 to about 3300 kg mm^{-2} for Film 2. Figure 15 is a typical SEM micrograph of a fractured DLC film cross section deposited on a Si substrate. All produced films were very dense, free of porosity or other volume defects and had a very uniform microstructure. Good continuity observed across the Si/DLC interface is indicative of the high adherence between Si and DLC films, which has been verified recently by adhesion strength experiments [52].

Auger spectra obtained from the as coated DLC specimens were all consistent with the spectra for amorphous graphite indicating a fine structure, as shown in Fig. 16 [53]. Narrow window AES scan about the C (KVV) peak at about 265 eV showed that the difference between the DLC films and graphite is that the shoulder at about 250 eV in the DLC films is not as pronounced as in graphite. This is a typical characteristic of IBD DLC films [53].

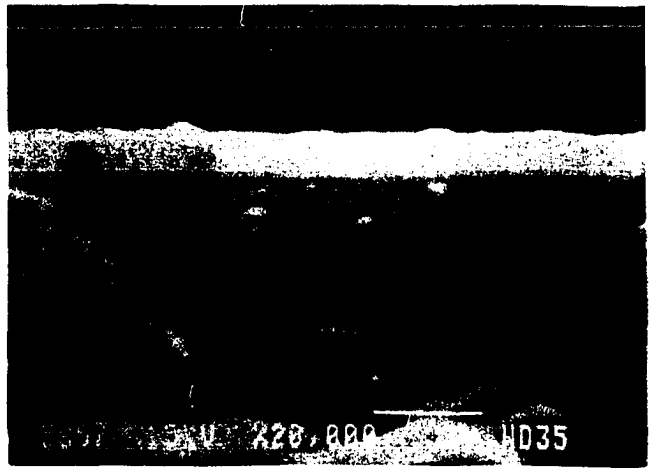

Figure 15 Scanning electron micrograph of a DLC film cross section.

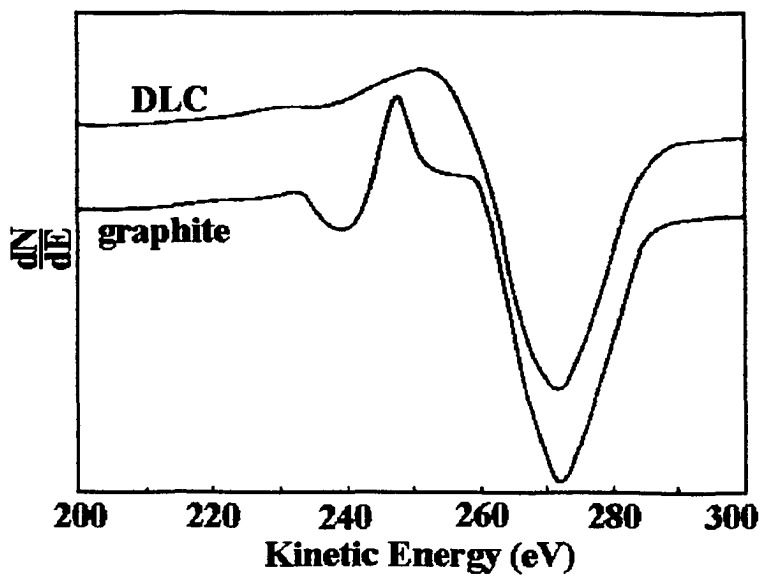

Figure 16 Auger spectra of a typical DLC film and graphite.

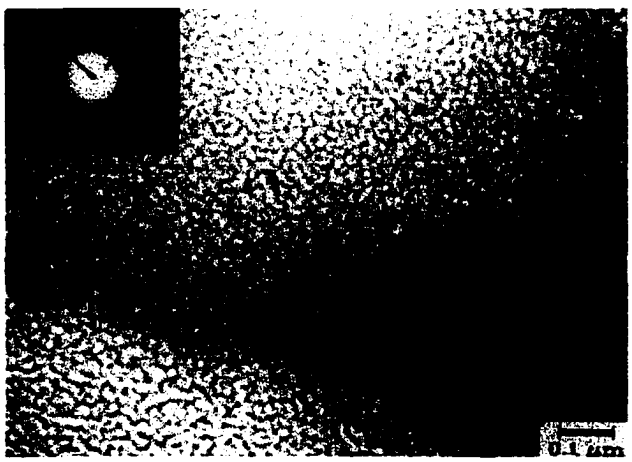

Figure 17 Bright field transmission electron micrograph of a DLC film.

TEM was used to obtain more detailed microstructural information about the DLC films. As can be seen in Figure 17, their microstructure can be described as a three-dimensional network of domains with a mean grain size of about 25 nm. The amorphous nature of the deposited DLC films was confirmed by the presence of diffuse ring electron diffraction patterns, Fig. 17. Only two diffraction rings were visible in the present DLC films with an approximate *d*-spacing of 2 Å and 1.125 Å, respectively. These results are in good agreement with those reported previously for amorphous diamondlike carbon deposited by RF glow discharge [54, 55]. There are obvious similarities among diffraction patterns of all amorphous carbon films [55-59] and Anderson [54] has argued that the amorphous structure can not be unquestionably identified since the principal graphite and diamond peaks are not very different. However, the measured *d*-spacing for the two rings in the present study is suggesting a diamondlike structure considering that the (111) and (220) are the strongest reflections for crystalline diamond corresponding to a *d*-spacing of 2.06 Å and 1.26 Å, respectively.

Also, the central spot in the diffraction patterns was larger than usual and it is possible that the strongest (00.2) reflection of graphite was present as a diffuse halo (d = 3.4 Å) encircling the central spot. Even though other, much weaker, reflections are missing in the diffraction image graphitic domains may also be present in the films.

Infrared spectroscopy was used to analyze the C-H bonding configuration and to estimate the ratio of sp^3 to sp^2 C-H bonds in the DLC films. First, IR transmission spectroscopy was performed on DLC films (about 500 Å in thickness) deposited onto NaCl substrates to allow a study of the film nature at the initial stages of development, as shown in Fig. 18 (a). A strong broad band was observed at about 2900 cm^{-1} due to C-H stretch vibrations, indicating relatively high hydrogen content in the films [20, 21]. Another evidence of C-H bonds is a strong band near 1450 cm^{-1}. A moderately strong feature at 1160 cm^{-1} can be assigned to sp^3 C-C vibrations. The weak absorption features at about 1560 cm^{-1} and 1260 cm^{-1} are due to sp^2 >C=C< bonds and mixed sp^2/sp^3 C-C vibrations, respectively. The band near 1730 cm^{-1} probably corresponds to carbonyl groups and the absorption at about 1380 cm^{-1} more than likely is due to graphitic bonds. IR spectra obtained from graphite in the present study showed a sharp strong absorption at about 1384 cm^{-1}. The weak absorption features at the lower wavenumbers of the spectrum correspond to various sp^2 and sp^3 configurations.

Figure 18 (b) shows the deconvolution of the C-H stretching region and Table 2 summarizes the various stretching modes present and the IR relative intensities. It has been previously reported that the sp^2 C-H bonds in this region show absorption at about 3060 cm^{-1} (aromatic) and 3000 cm^{-1} (olefinic). However, neither one of these features were observed for the 500 Å thick DLC films deposited on NaCl substrates. This

stretching region mainly showed the presence of sp^3 C-H vibrations which is in agreement and further supports the electron diffraction observations. If at all present, the sp^2 type bonds in these films may be associated with sp^2 C-H_2 (olefinic) bonds and graphitic bonds at 1450 cm^{-1} and 1380 cm^{-1}, respectively.

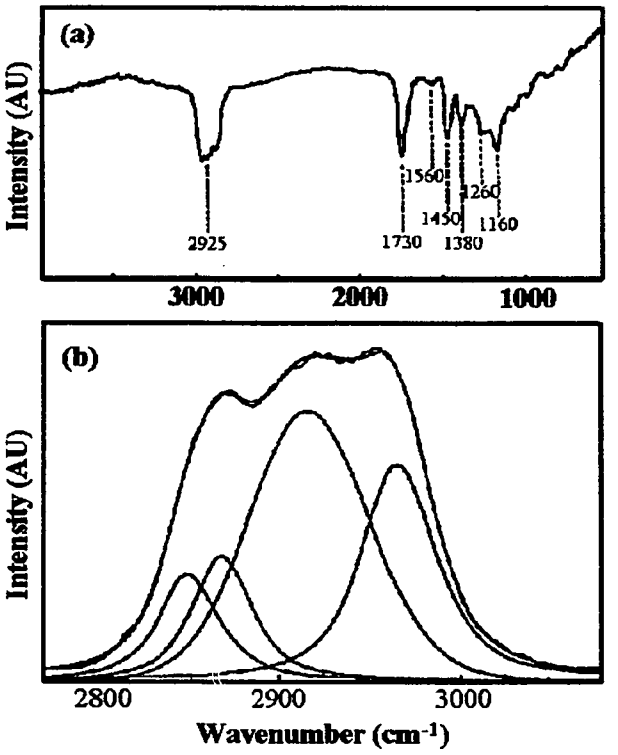

Figure 18 (a) Infrared transmission spectrum of a DLC film deposited on a NaCl substrate, and (b) deconvolution of the C-H stretch vibrational absorption region.

Infrared reflectivity was used to estimate relative amounts of sp^3 and sp^2 carbon-bonded hydrogen in the DLC films with the two different Si interlayers (Film 1 and Film 2). Very similar IR spectra were obtained from these two films and their main features were in general agreement with those reported earlier for typical DLC films [21, 60]. Figures 19 (a) and (b) show the curve fitted absorption band due to C-H stretch

vibrations in the 2700-3400 cm^{-1} region for these two films. Table 2 presents the peak position, type of bond and relative intensity of the peaks composing this band. The relative amount of each bonding type present was obtained by estimating the area under each peak. As shown in Figure 19, bonds at 2870, 2920 and 2970 cm^{-1} make the largest contribution in this band. The ratio sp^3/sp^2 was found to be approximately 3.2 and 4.1 for Films 1 and 2, respectively. Ratios of about 3.5 have been reported previously for typical IBD DLC films [61].

Table 2 Relative contributions of absorption peaks in the C-H stretching region.

Wavenumber (cm^{-1})	Assignment	Peak Contribution, %		
		Film 1	Film 2	DLC/NaCl
2850 2855	sp^3 C-H_2 sp^3 C-H	0.5	0	12
2870	sp^3 C-H_3	29.2	39.7	13
2920-5	sp^3 C-H_2 sp^3 C-H	32.4	28.6	47
2970	sp^3 C-H_3	14	12.2	28
3000	sp^2 C-H	19.2	16.6	0
3060	sp^2 C-H	4.7	2.9	0

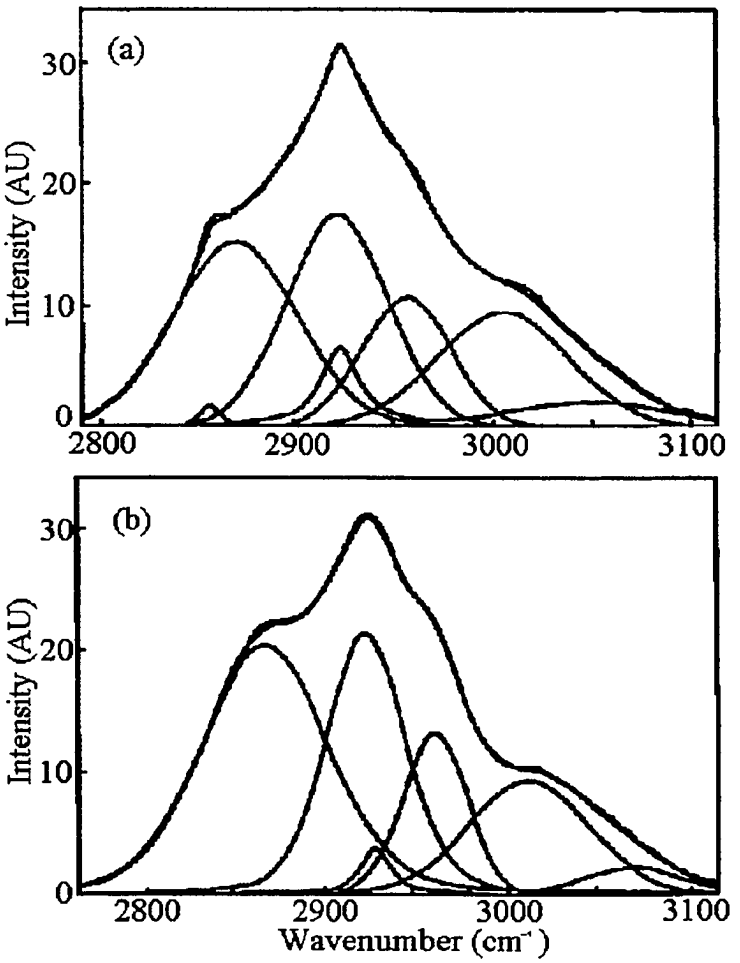

Figure 19 Deconvolution of the C-H stretch absorption from DLC (a) Film 1 and (b) Film 2.

The higher sp^3/sp^2 ratio determined by FTIR for Film 2 seems to be in agreement with the somewhat higher hardness obtained for this DLC film. Finally, the IR results (Figures 17 and 18) suggest that at the initial stages of deposition the sp^3 C-H bonds are dominant, and a substantial sp^2 C-H bonding evolves as the films grow in thickness.

Raman spectra are sensitive to changes in translational symmetry, and can be used to study the disorder or crystallite formation and structural modifications in DLC films. The first order Raman spectrum for diamond and graphite consists of a single line

at 1332 cm^{-1} and at about 1580 cm^{-1} (G), respectively. In disordered graphite, which lacks the long-range-translational symmetry, the crystal momentum need no longer be conserved and the spectrum changes drastically. The most dramatic effect is that in addition to G band, another disorder or "D" broad line appears at about 1355 cm^{-1}, which is also associated with in-plane vibrations [1, 14, 62-66].

Typical Raman spectra for the DLC films are presented in Figure 20, and they are similar to those of DLC films reported previously. The parameters of the gaussian line shape analysis for the above spectra are summarized in Table 3. Both spectra are characterized by features at about 1555 cm^{-1} and the broad shoulder line at about 1370 cm^{-1}. As has been shown conclusively by Wagner *et al* [67], the downshift in the G band in DLC films containing both sp^3 and sp^2 carbon bonds arises from the used incident photon energy of 2.41 eV (excitation wavelength 514.5 nm). As has been reported, increasing the incident photon energy from 2.18 eV to 3.5 eV an increase in the G frequency is produced due to a resonant enhancement of the Raman efficiency of the high-frequency vibronic excitation [68].

The broad band at about 1370 cm^{-1}, Figure 20, is in agreement with the observations for disordered graphite. The intensity of this band (I_D) has been found to be related to the crystallite size in the film. More specifically, a linear relationship has been established between the intensity ratio I_D/I_G and the reciprocal of the grain size that was obtained by x-ray diffraction broadening measurements [69]. Assuming that such an analysis would be valid here, it would have produced a grain size of about 24 nm and 17 nm for Films 1 and 2, respectively. This is in good agreement with the grain size determined by TEM in DLC films deposited on NaCl substrates (~ 25 nm). Film 1 and

the DLC/NaCl film can be considered similar since both were developed on an e-beam deposited Si interlayer. The smaller grain size of Film 2 may be attributed to an enhanced DLC nucleation due to the presence of a rougher Si interlayer surface produced under the 1 keV Ar^+ bombardment. This is in agreement with the established practice of scratching the substrate surface (ultrasonically or fine polishing) prior to diamond film deposition. A rougher substrate surface has been found to significantly enhance the nucleation of diamond crystals (sp^3-bonded carbon), probably due to a higher density of nucleation sites.

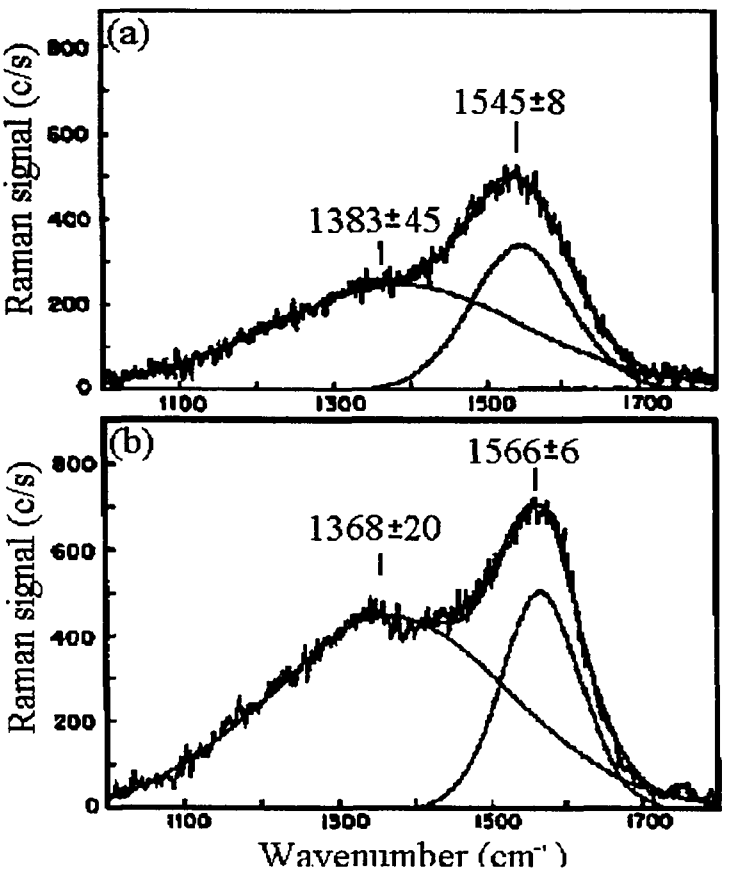

Figure 20 Raman spectra of as-deposited DLC (a) Film 1 and (b) Film 2.

Table 3 Characteristic parameters of Gaussian line shape analysis of Raman spectra.

Film	ν_D position cm^{-1}	Γ_D (FWHM) cm^{-1}	I_D (Intensity) a.u.	ν_G position cm^{-1}	Γ_G (FWHM) cm^{-1}	I_G (Intensity) a.u.	I_D/I_G
#1	1383(45)	393(30)	100699	1545(8)	150(15)	54508	1.8
#2	1368(20)	367(19)	172815	1566(4)	123(9)	65956	2.6

Resonant Raman experiments [67] and IR spectroscopy results [70] from the same DLC films have shown that Raman spectra can be described by a heterogeneous structural model involving two phases (differing in their electronic and vibronic properties). According to this model [67], the high frequency band in DLC Raman spectra is assigned to a graphitelike sp^2-bonded phase and the low-frequency band to the sp^3-bonded phase (and any probable contributions from the graphitelike D band). The above concept is consistent with a model [60] proposed to describe the DLC structure and explain the relatively low optical band gap observed in these films in spite the presence of a large fraction of diamondlike sp^3-bonded carbon. According to this model, sp^2-bonded carbon segregates in small graphitelike clusters composed of at least four fused six-fold rings (for example an optical gap of 1.3 eV corresponds to graphitic clusters consisting of about twenty fused six-fold rings) that are interconnected by sp^3-bonded carbon.

At first view, this model seems consistent with the rather uniform appearance and the network structure observed by TEM in the present DLC films. Also, according to the above model, comparison of the intensity ratios of the Raman spectra can allow

us to speculate that Film 2 has a higher fraction of sp^3-bonds than Film 1 (ratio of 2.6 *vs* 1.8). This result is in general agreement with the IR observations (Figure 19 and Table 2) that also showed a larger sp^3-bond fraction present in Film 2. Also, a relative comparison between the ratios describing the sp^3/sp^2 fractions in Films 1 and 2 obtained by IR and Raman spectroscopy shows approximately values of 1.3 (4.1/3.2) and 1.4 (2.8/1.8), respectively. Thus, it seems that there is good agreement between these two techniques used to describe the relative sp^3/sp^2 fractions. The slightly higher ratio obtained by Raman spectroscopy (1.4) may be attributed to D line contributions to the low-frequency band of the spectrum as discussed by Wagner *et al* [67].

5.1.2 Characterization of Si-DLC Films

Table 4 summarizes the processing parameters and characteristics of the Si-DLC films. It can be seen that the ion current density plays a vital role in the resulting parameters of the films. Generally, the increased current density resulted in higher deposition rates. As can be seen from Table 4, R_a values for all films are lower than the film thickness, indicating the existence of continuous DLC coating on the substrate. All films exhibited high hardness although lower than previously reported for DLC films (Si-free) of the same thickness [13]. The highest hardness value exhibited by Film 1 in spite of its low thickness, suggests a more diamond-like character, which may result from the low ion current density used during the deposition process, as will be discussed later. Similar processing trends where higher power densities during deposition of DLC films increase deposition rates but induce graphitization have been reported in the literature [5].

Table 4: Characteristics of the Si-DLC films.

Sample	Processing Conditions	Thickness (μm)	Average Roughness R_a(nm)	Microhardness H_K
Film 1	50 kV, 85 μA cm^{-2} 250 min	0.6	46.2	1760
Film 2	50 kV, 143 μA cm^{-2} 335 min	1.4	19.6	1325
Film 3	50 kV, 163 μA cm^{-2} 240 min	3.5	145.4	1425
Film 4	40 kV, 100 μA cm^{-2} 240 min	0.5	16.8	1430
Film 5	40 kV, 195 μA cm^{-2} 195 min	2.2	42.3	1140

SEM examinations of fractured cross sections showed uniform and featureless films, without porosity or other visible defects, Figure 21. Also, separation or gaps between the coating and the substrate were not detected suggesting good film adhesion. It has been previously reported that DLC films exhibit excellent adhesion to Si and Si interlayers are routinely used to improve DLC adhesion on metallic substrates [52]. TEM analysis of the as-deposited films showed the presence of diffuse rings indicative of the amorphous nature of the films. As has been observed previously, diffraction patterns of DLC films exhibit mainly two characteristics. First, two diffuse rings with *d*-spacing consistent with the (111) and (200) diffractions of crystalline diamond, suggesting the presence of a short-range order crystalline but defected structure. Second, a diffuse halo encircling the central spot arising from the strong (00.2) sp^2 graphite reflection [71-74]. It should be noted that the intensity of the halo varied for the different Si-DLC films being higher for Film 3 and lower for Film 1 suggesting a variation in the sp^3/sp^2 ratio for these films. These results indicate a mainly amorphous

structure where domains with sp^3 and sp^2 bonding exist. However, it has been pointed out [52] that electron diffraction patterns alone are insufficient to deduce the presence of diamond or graphite phases in mostly amorphous structures, since the difference between the interplanar spacing of cubic diamond and textured graphite is small.

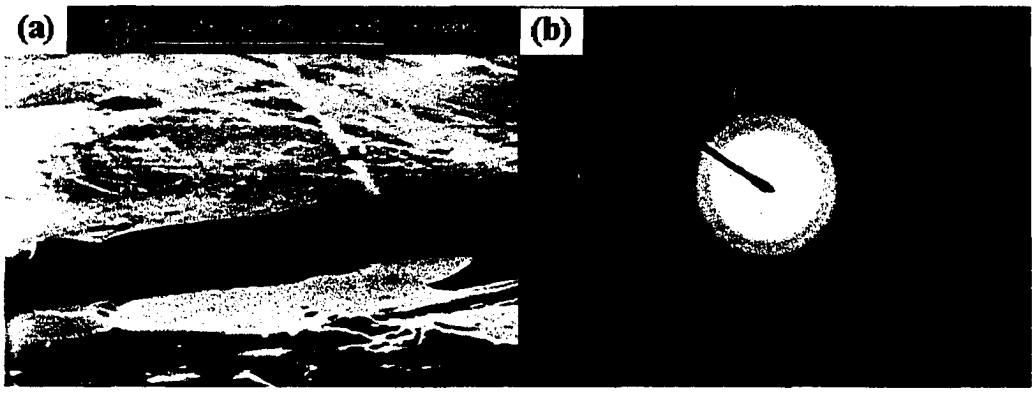

Figure 21 (a) Scanning electron micrograph and (b) an electron diffraction pattern of a Si-DLC film (Film 3).

IR absorption spectroscopy was used in this study to obtain information about C-H and C-C bonding configuration in the Si-DLC films, the ratio of sp^3/sp^2 bonding, and the role of Si in the film structure. The spectra collected for these films demonstrate some features that are typical for most conventional DLC films as well as some unique features that have not been observed in Si-free DLC films [13]. Figure 22 shows infrared absorption spectra of Films 1-5.

A strong, broad band at about 2800-3100 cm^{-1} has been observed for numerous DLC films and usually indicates relatively high hydrogen content of the films. It is composed of C-H stretch vibrations and includes a number of sp^3 and sp^2 C-H stretching modes (Table 5). In this study, the C-H stretching region was used to determine relative amounts of sp^3 and sp^2 bonding types in DLC films. Figure 23 shows

the curve fitted infrared absorption spectra from C-H stretching vibrations in Si-DLC films.

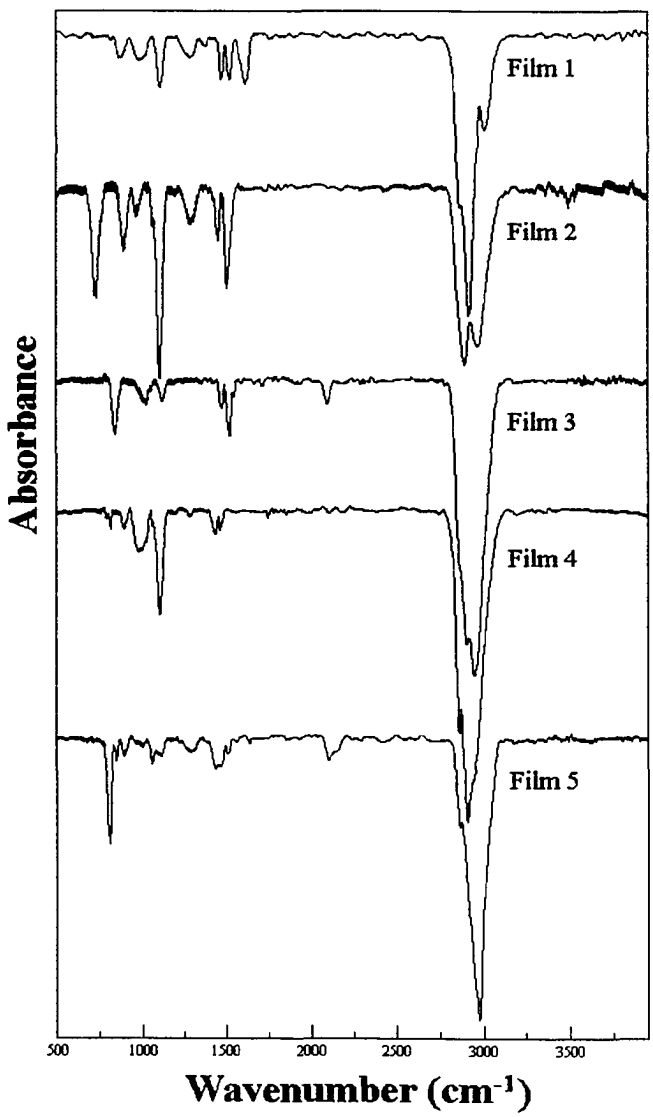

Figure 22 Infrared transmission spectra of Si-DLC films.

Table 5 presents the peak position, bonding type and relative intensity for each peak contributing to the C-H band. As can be seen from Fig. 23, peaks that correspond to sp^2 C-H bonds (2945, 3000 and 3025 cm^{-1}) make a significant contribution in Films 3 and 5, while in Film 1, 2, and 4, sp^3 C-H peaks (2860, 2920, and 2970 cm^{-1}) dominate the absorption spectrum. None of the films exhibited the aromatic C-H mode at 3060 cm^{-1}. The relative amount of each bonding type was obtained by estimating the area under each peak, and the sp^3/sp^2 ratio of the films varied between 1.5 (Films 3 and 5) to 5.4 (Film 1), as shown in Table 5. The much higher value calculated for Film 1 is in agreement with the TEM results and the highest hardness obtained for this film. It should be noted that the accuracy of sp^3/sp^2 bonding ratio as determined by FTIR has been questioned [7]. Jager et al. [12] has suggested recently that a higher portion, about 35 %, of sp^3 bonded atoms are hydrogenated, while for sp^2 bonded atoms this portion is only 20 %. Therefore, the absolute values of the sp^3/sp^2 ration obtained from IR spectroscopy may be less important than the relative values for different samples as a means to study the effect of various deposition parameters on the film structure.

As can be seen from Figure 23 and Table 5, in specimens 4 and 5, processed at lower ion energy, relative contribution of $C-H_3$ groups to the total absorption by sp^3 coordinated sites compared to $C-H_2$ and C-H groups is much higher than in samples 1-3. This indicates a higher degree of dissociation of the $C-H_3$ groups by ion bombardment at higher energies. Similarly, absorption by the sp^2 sites in the C-H stretch region in Films 4 and 5 is produced exclusively by $C-H_2$ bonds, with C-H peak at 3000 cm^{-1} appearing only in Films 1-3, its intensity slightly increasing with increased current density but still lower than that of the $C-H_2$ peak. Increasing the ion current

density also significantly affects the film structure, which is most evident from the dramatically decreasing intensity of the sp^3 peak at 2920 cm^{-1} and the increasing intensity of the sp^2 peak at 2945 cm^{-1}, as well as the overall decrease in the sp^3/sp^2 ratio of the films.

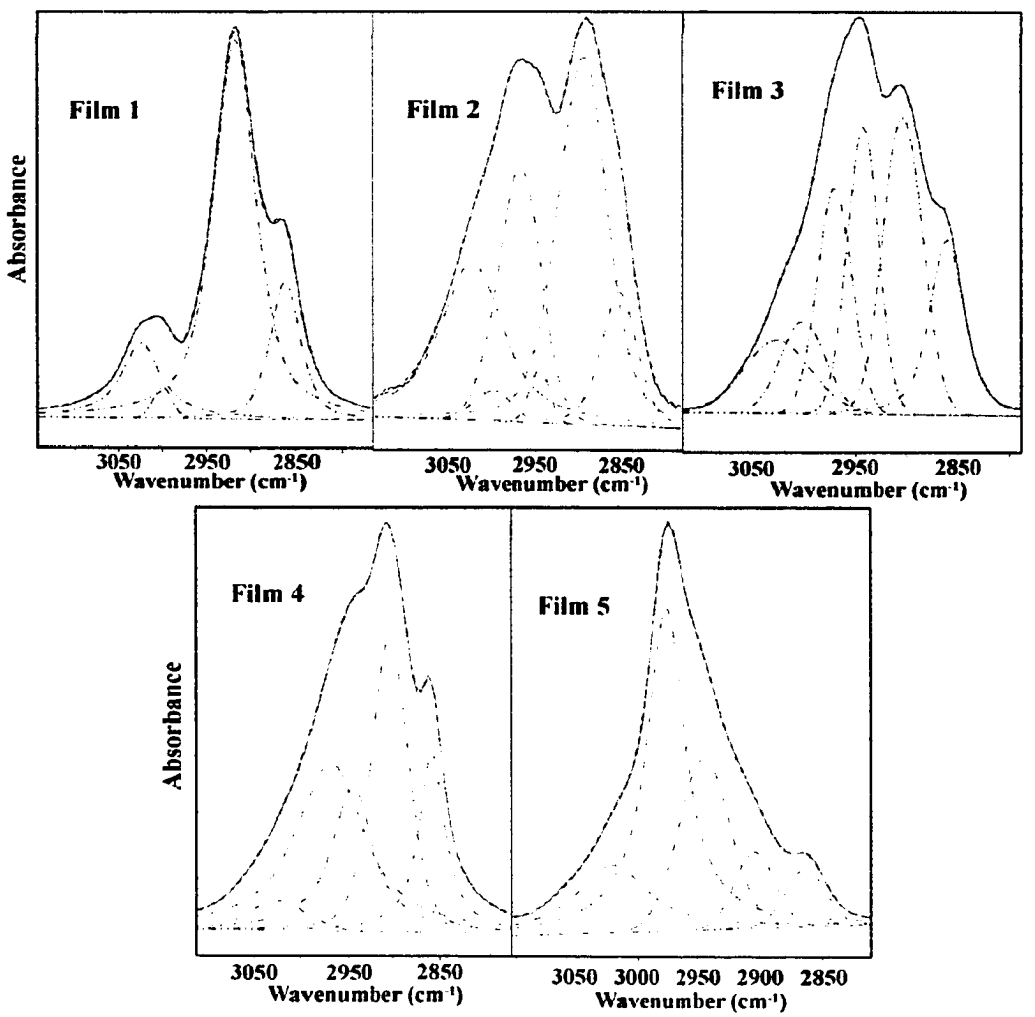

Figure 23 Deconvolution of the C-H stretch absorption band of Si-DLC films.

Table 5 IR vibrational mode assignments in the C-H stretch region for Si-DLC films [5, 70, 75, 76].

Wavenumber (cm^{-1})	Assignment	Peak Contribution, %				
		Film 1	Film 2	Film 3	Film 4	Film 5
2860	sp^3 C-H, C-H_2, C-H_3	16.8	10.3	16.0	15.1	6.0
2900 to 2920	sp^3 C-H_2, C-H	67.6	39.4	26.2	28.4	8.0
2945	sp^2 (olef) C-H_2	0.0	2.1	20.3	19.0	23.8
2970	sp^3 C-H_3	0.0	22.5	17.2	33.4	46.4
3000	sp^2 (olef) C-H	2.0	2.3	9.2	0.0	0.0
3025	sp^2 (olef) C-H_2	13.6	23.4	11.1	4.1	15.8
sp^3/sp^2		**5.4**	**2.6**	**1.5**	**3.3**	**1.5**

Another strong feature near 2100 cm^{-1} appears only in the samples deposited at the highest current density values (Films 3 and 5) and can be attributed to Si-H stretching mode [77, 78]. These features have not been observed in our previous study since no Si was present in the DLC films. The Si-H deformation bands usually appear along with Si-H stretch band in the 800-950 cm^{-1} region. Therefore, moderately strong peaks centered around 845 cm^{-1} and observed only in Films 3 and 5 can be assigned to Si-H deformation modes [75, 77]. However, in Films 1, 2, and 4, the peak centered at approximately 870-890 cm^{-1} more than likely appears due to sp^3 C-C bonds [5, 76], since the Si-H stretch at 2100 cm^{-1} was not present in the spectrum.

Moderately strong peaks in the 970-1010 cm^{-1} area observed in Films 1, 2, and 4 have been reported previously for a-$Si_{1-x}C_x$:H films [75, 79] and are due to CH_n and Si-CH_3 deformation modes. This band is shifted to the 1020-1050 cm^{-1} typical for Si-CH_2 deformation modes in Films 3 and 5.

A strong band centered around 1110 cm^{-1} which was observed in all samples resulted from Si-O-C or Si-O-Si bonds [77], although its intensity was significantly reduced in Films 3 and 5 where the current density was relatively high. This may

indicate that the siloxane backbone (Si-O-Si-O-Si) of the precursor molecule remains partially intact during the ion bombardment process and becomes incorporated into the DLC structure. It should be noted that $Si-C_6H_5$ bond, present in the precursor molecules, absorbs strongly in the 1430 and 1110 cm^{-1} regions [77] and thus may contribute to the 1110 cm^{-1} band, especially in the second group (Films 4 and 5) where the 1430 cm^{-1} peak was observed.

A moderately strong peak at 1470 cm^{-1}, present in all films, may be assigned to CH_2 and CH_3 deformation bands [75], and a broad band at 1240-1300 cm^{-1} probably corresponds to mixed sp^2/sp^3 C-C bonds [5, 76]. A strong peak at 1515-1520 cm^{-1} was observed only in the first group samples (Films 1-3), and corresponds to mixed sp^2/sp^3 C-C bonds [5, 76]. Some features were observed only for Film 1, including a small peak at 1370 cm^{-1} which is likely due to sp^3 C-H bend [76], and the peak at 1620 cm^{-1}, usually assigned to C=C olefinic stretching in a-C:H as well as a-$Si_{1-x}C_x$:H films [5, 70, 75, 76].

These results indicate that Si is participating in the structure of DLC by tetrahedral bonding with hydrogen and CH_n groups, which leads to significant differences in the IR absorption spectra of Si-DLC and conventional DLC films. Incorporation of Si in DLC structure seems to suppress the formation of aromatic structures, which are often observed in DLC films, and to promote the formation of sp^3 bonds at low current density conditions (Film 1), producing much higher sp^3/sp^2 ratio than previously observed for DLC films [13]. Furthermore, low current density conditions seem to favor the participation of Si in tetrahedral Si-C bonds, thus producing more diamond-like behavior and increased hardness, while increased current density promotes the

formation of Si-H bonds, resulting in softer coatings. The existence of Si-H bonds, rather than Si-C bonds, at increased power density processing conditions (Films 3 and 5), is consistent with the fact that Si-C bonds are thermodynamically less stable than Si-H bonds [75].

5.1.3 Modeling of the DLC structure

The ability of carbon to form strong chemical bonds under a variety of coordination numbers (from 2 to 4) is responsible for the unique properties of noncrystalline carbon phases, and at the same time makes the system very complex. Carbon can form sp^3, sp^2, and sp^1 bonds, each of which may be present to varying extents in DLC films depending on deposition conditions and hydrogen content. The C-C nearest neighbor distance, the coordination number, and the C-C-C bond angle can be expected to differ significantly from one structure to another. For the unhydrogenated a-C films, it seems likely that configurations similar to those in the crystalline forms of carbon, diamond and graphite, will occur. In sp^3-hybridized diamond each carbon atom is tetrahedrally coordinated with a 109.5° bond angle and a bond length of 1.544 Å, and sp^2-hybridized graphite has a planar trigonal bonding with a 120° bond angle and a bond length of 1.421 Å. In the presence of hydrogen, a great number of bonding configurations can be imagined, with bond lengths ranging from 1.20 Å (triple bond) to 1.55 Å (single bond) and bond angles from 180° (two unsaturated adjacent C-C bonds) to 60° (as in cyclopropane).

Due to the presence of sp^2 sites, the electronic structure of amorphous carbon and the effect of disorder is very different from other well-studied systems, such as a-Si.

For a group IV element at an sp^3 site, all four valence electrons lie in sp^3 hybrid orbitals and form σ bonds with neighbors. At an sp^2 site, only three of these electrons form σ bonds, while the fourth enters a π orbital normal to the σ bonding plane. The importance of the π states is that they are only weakly bonding so that they usually lie closest to the Fermi level. They will therefore form both the valence- and conduction-band states in a-C and a-C:H [11].

It has been demonstrated experimentally that deposition of hard a-C:H, or DLC, films requires energetic ion bombardment of typically above 100 eV, which results in large fractions of diamond-like sp^3 bonds instead of the energetically favored sp^2 configuration. Therefore, nonequilibrium ion-beam-induced processes may be the cause of formation of tetrahedral bonding. Recently, qualitative arguments have been considered for the possible importance of the preferential removal of graphitic carbon atoms versus carbon in a diamond lattice [80]. In graphite, recoil atoms generated in collision cascades produced by the incident ions will become permanently displaced at initial energies above the average displacement threshold of about 25 eV, while this displacement threshold is about 80 eV in diamond. Therefore, the formation of sp^3 sites will be favored in a certain range of incident energies. Moller [80] reported that TRIM and TRIDYN simulation based on the preferential displacement model predicted an increase in the sp^3/sp^2 ratio between 30 eV and 1 keV in agreement with experimental data, but failed to explain a decrease towards higher energies. A similar effect is observed in this work, where an increase in the ion beam current density produced a decrease in the sp^3/sp^2 ratio instead of the opposite effect that could be expected based

only on the preferential removal mechanism. It should be noted that the effect of increased current density on the structure of DLC films studied in the present work was similar to that of the well-studied annealing process, resulting in partial graphitization of the films. This may indicate that the heating of the films caused by ion-beam irradiation may become important under high energetic flux conditions.

Experimental results discussed above demonstrate the presence of both diamond-like sp^3 and graphite-like sp^2 bonding types in the films, although at this point it is not clear whether sp^3 and sp^2 sites are randomly distributed in a homogeneous amorphous structure, or segregate into separate diamond-like and graphite-like domains. Analysis of the various possible configurations based on the band gap and total energy considerations reported by Robertson and O'Reilly [11] suggests that the sp^2 sites will tend to form compact clusters of fused sixfold rings. Akkerman et al. [81, 82] have argued that at low temperature conditions, chemical ordering will tend to separate the a-C:H into two structures, amorphous networks of sp^2 and sp^3 bonded carbon. An increase in the deposition temperature (to approximately 250 °C) will eliminate this phase separation due to entropy effects, and make possible a variety of mixed bonding units, i.e., $C(sp^3)$-$C(sp^2)$. Therefore, in the presence of a graphitic structural component, visible in the IR absorption spectra as aromatic sp^2 carbon bonds, the film structure can be expected to consist of small graphite-like clusters composed fused six-fold rings, interconnected by areas of sp^3-bonded carbon, as described in numerous previously suggested models discussed above. This model of DLC structure is in good agreement with experimental observations for the ion-beam deposited DLC films (Si-free) studied in this work. In the case of Si-DLC films, however, no aromatic

structures were observed and there is no evidence of clustering of the sp^2 coordinated carbon atoms, therefore other structural models should be considered. Experimental results obtained for the Si-DLC films are consistent with a structure consisting of an sp^2-sp^3 carbon network with the $C(sp^2)$ atoms present in olefinic rather than aromatic bonding units. This network mainly consists of two fundamental structural units, namely $C(sp^3)$-centered tetrahedral and $C(sp^2)$=$C(sp^2)$-centered planar bonding units. Each of these units has four remaining bonds available to bond to the network, and they are likely to be distorted from their ideal tetrahedral or planar structures due to their incorporation in the disordered network. The network also incorporates statistically distributed CH_n groups, with the relative fractions of C-H, $C-H_2$, and $C-H_3$ bonding units determined by the deposition parameters (ion beam energy and current density). The sp^3 $C-H_3$ bonding serves as the terminating bonding in this network and helps relieve stresses associated with the distortion of the bond lengths and angles.

Tetrahedrally coordinated Si atoms may be present at any sp^3-coordinated site of this network instead of a $C(sp^3)$ atom. It is suggested that the presence of these atoms may serve as an inhibitor of the formation of aromatic groups. Another important factor preventing aromatic clustering in these films may be the ion mixing effect produced by the high energy (40 and 50 keV) Ar^+ ion beam bombardment during film deposition. If, in fact, some clustering of the sp^2 sites does occur, the graphitic component of the films can be described as an $C(sp^2)$=$C(sp^2)$ unit bonded to four other $C(sp^2)$=$C(sp^2)$ units, without the formation of aromatic or graphitic rings. The proposed structure is shown as a two-dimensional schematic network in Figure 24. It includes four types of atoms:

$C(sp^3)$, $C(sp^2)$, H, and Si, and corresponds to $sp^3/sp^2 \approx 2$. As discussed above, there are no aromatic or graphitic six-fold rings, minimal clustering of the $C(sp^2)$ atoms, and no phase separation into distinct sp^2 and sp^3 regions. Instead, both $C(sp^3)$ and $C(sp^2)$ atoms are incorporated into an amorphous mixed diamond-graphitic phase, with Si atoms substituted for carbon atoms at random sp^3-coordinated sites. The network shown here is terminated at the boundaries by dangling bonds, which in a film would be bonded to other atoms.

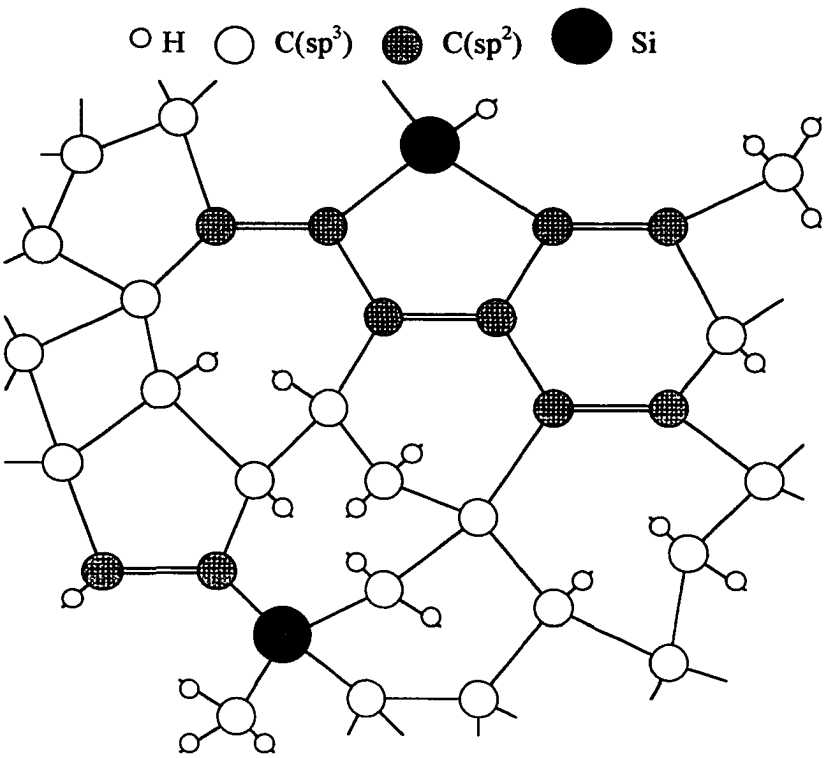

Figure 24 A proposed schematic bonding network for Si-DLC films. Four types of atoms are shown: $C(sp^3)$, $C(sp^2)$, H, and Si.

5.2 Effect of Flux Energy on Outer Layer Structure of Plasma Nitrided Surfaces

5.2.1 Sample Preparation

In this study, two groups of titanium specimens were nitrided at different conditions in order to investigate the roles of energetic ions and neutrals and the effect of the particle energies on the nitriding process. All specimens were polished, ultrasonically cleaned in methanol and dried in air prior to surface treatment.

The first group included six Ti specimens that have been processed by IPAP at the current densities ranging from $j_1 = 0.5$ mA cm^{-2} to $j_6 = 3.0$ mA cm^{-2}, at pressure p = 50 mTorr and bias voltage $V_c = 2000$ V. The second group included three specimens that were nitrided at lower plasma energy conditions, approaching those encountered in conventional plasma nitriding. This group was processed at the same bias voltage as the previous specimens, with current density controlled between $j_7 = 0.5$ mA cm^{-2} and $j_9 =$ 1.5 mA cm^{-2} by adjusting the chamber pressure. Processing time of three hours was used for both groups of specimens, which we expected to allow to reach the steady state and develop the structure typical for each particular set of the processing parameters.

This choice of processing parameters resulted in a wide range of values for the L/λ ratio and, accordingly, the average ion and neutral energies. For IPAP specimens, they varied from L/λ =5.25, E_i^a=616 eV and E_n^a=263 eV in specimen 1, to L/λ =2.16, E_i^a=1077 eV and E_n^a=428 eV in specimen 6. Processing conditions for the second group of specimens produced much higher L/λ values, with L/λ as large as 22.7 for specimen 9, resulting in relatively low ion and neutral energies, about 170 and 81 eV,

respectively. The calculated values of the processing parameters for both groups of specimens are summarized in Table 6.

Table 6 Processing parameters and calculated energies and dose levels.
* Diode (conventional) processing

Sample	Pressure, mTorr	Current Density, A m^{-2}	L/λ	E_i[a], eV	E_n[a], eV	Ion Dose	Neutral Dose	Total Dose (part cm^{-2})*10^{20}
1	50	5	5.25	616	263	0.3	1.8	2.1
2	50	10	3.72	793	325	0.7	2.5	3.2
3	50	15	3.04	905	361	1.0	3.1	4.1
4	50	20	2.63	984	386	1.3	3.6	4.9
5	50	25	2.35	1045	406	1.7	3.9	5.6
6	50	30	2.16	1077	428	2.0	4.3	6.3
7*	170	5	17.9	211	100	0.3	6.0	6.3
8*	290	10	21.6	177	84	0.7	14.6	15.3
9*	370	15	22.5	170	81	1.0	22.7	23.7

The IPAP specimens processed at high current densities (5 and 6) had the golden-yellow color typical for FCC TiN. The surface color changed to pale yellow and then silverish as the current density decreased, indicating lower amounts of the stoichiometric TiN phase present at the surface. The second group of specimens, 6 through 9, processed by conventional ion nitriding (high pressure, low current density), had much smoother surfaces than the IPAP specimens, which had rougher and duller appearance, probably caused by constant energetic particle bombardment during processing.

5.2.2 AES and SEM surface analysis

Prepared specimens were fractured in the working chamber, producing ductile transgranular fracture typical for titanium in the subsurface material in all samples (Figure 25). Brittle fracture of the surface layer was observed in the IPAP specimens,

Fig. 25, (a) and (b). This brittle layer very likely includes both TiN and Ti_2N layers, and its thickness can be estimated as approximately 3-5 μm. However, this brittle layer could not be detected in the specimens of the second group (Fig. 25 (c)), probably because of the very small layer thickness, and the fracture type of the nitrided layer in these samples could not be determined. As can be expected, IPAP samples show effects of plasma etching, which become more pronounced as the bombarding particle energies are increased (Figure 26, (a) and (b)). Samples of the second group, processed by conventional plasma nitriding, exhibit relatively smooth surface without significant traces of sputtering, which indicates that the energetic particle bombardment may not be a major factor in this process (Figure 26 (c)).

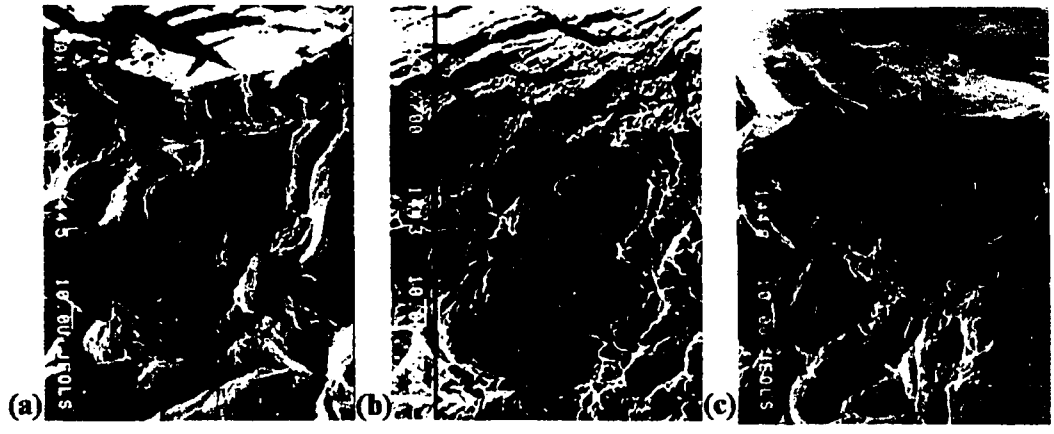

Figure 25 Scanning electron micrographs of the fracture surfaces of plasma nitrided samples processed by (a) IPAP at 2 mA cm^{-2}, (b) IPAP at 1 mA cm^{-2}, and (c) diode technique at 1 mA cm^{-2}.

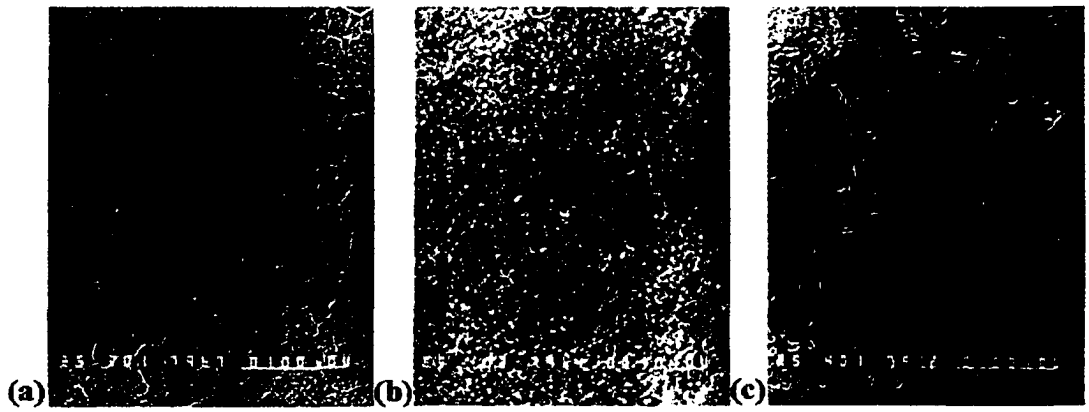

Figure 26 Scanning electron micrographs of the nitrided surfaces of samples processed by (a) IPAP at 2 mA cm^{-2}, (b) IPAP at 1 mA cm^{-2}, and (c) diode technique at 1 mA cm^{-2}.

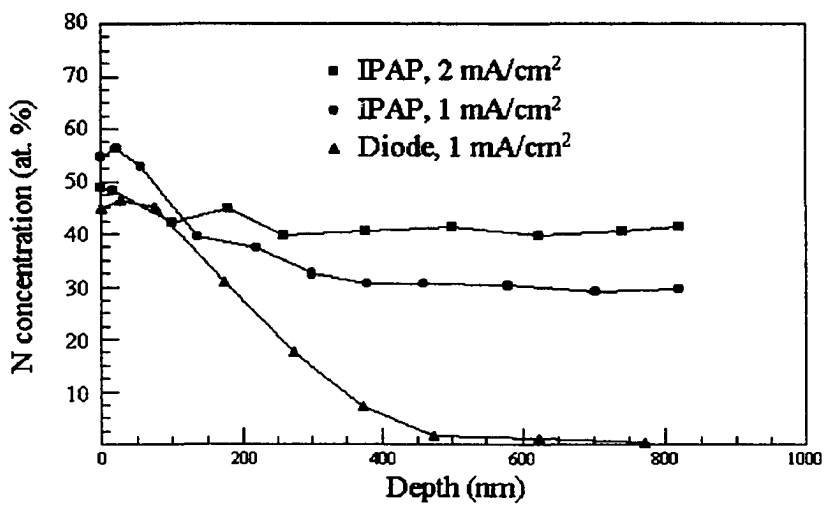

Figure 27 Nitrogen concentration profiles of plasma nitrided samples processed by IPAP at 2 mA cm^{-2}, IPAP at 1 mA cm^{-2}, and diode at 1 mA cm^{-2}.

The composition depth profiles of the processed specimens were measured by AES. Relative intensities were determined from peak-to-peak heights and elemental concentrations were calculated from these intensities by using the appropriate sensitivity factors. Figure 27 shows nitrogen concentration profiles for two IPAP samples prepared with current densities of 1 mA cm^{-2} and 2 mA cm^{-2} and one conventionally processed

sample prepared at 1 mA cm^{-2}. As can be seen from Figure 27, the nitrogen content at the surface is approximately 50 at. % for all samples. For the sample prepared with the conventional diode nitriding system, the nitrided layer is very thin (<500 nm), with the nitrogen content decreasing rapidly with increasing depth. For the IPAP samples the nitrided layer extends well beyond the range measure (800 nm), with nitrogen concentration remaining at a stable level (40-45 % for the 2 mA cm^{-2} sample) throughout the region measured.

5.2.3 EXAFS data analysis

EXAFS data analysis follows the previously described procedure and includes deglitching, background removal, normalization, Fourier transform, inverse FT, and curve fitting. The measured intensities are converted to absorption coefficient μ according to equation 16. Figure 28 shows total electron yield spectra of the samples produced by IPAP (a) and diode (b) nitriding, shown with the spectra of pure Ti metal and TiN powder. AUTOBK code was used for background removal and normalization of the spectra. Nonlinear least-squares fitting was performed using FEFFIT code, and theoretical standards used in fitting were produced by FEFF. Figure 29 shows k^1 weighted TEY EXAFS data, and corresponding Fourier transformed spectra are shown in Figure 30.

In FCC materials, such as TiN, the first peak in radial distribution corresponds primarily to single scattering, and the multiple scattering contribution is negligible. This can be demonstrated by comparing the position of the first peak in Fourier transformed spectra to the effective path lengths and relative path contributions listed in Table 7.

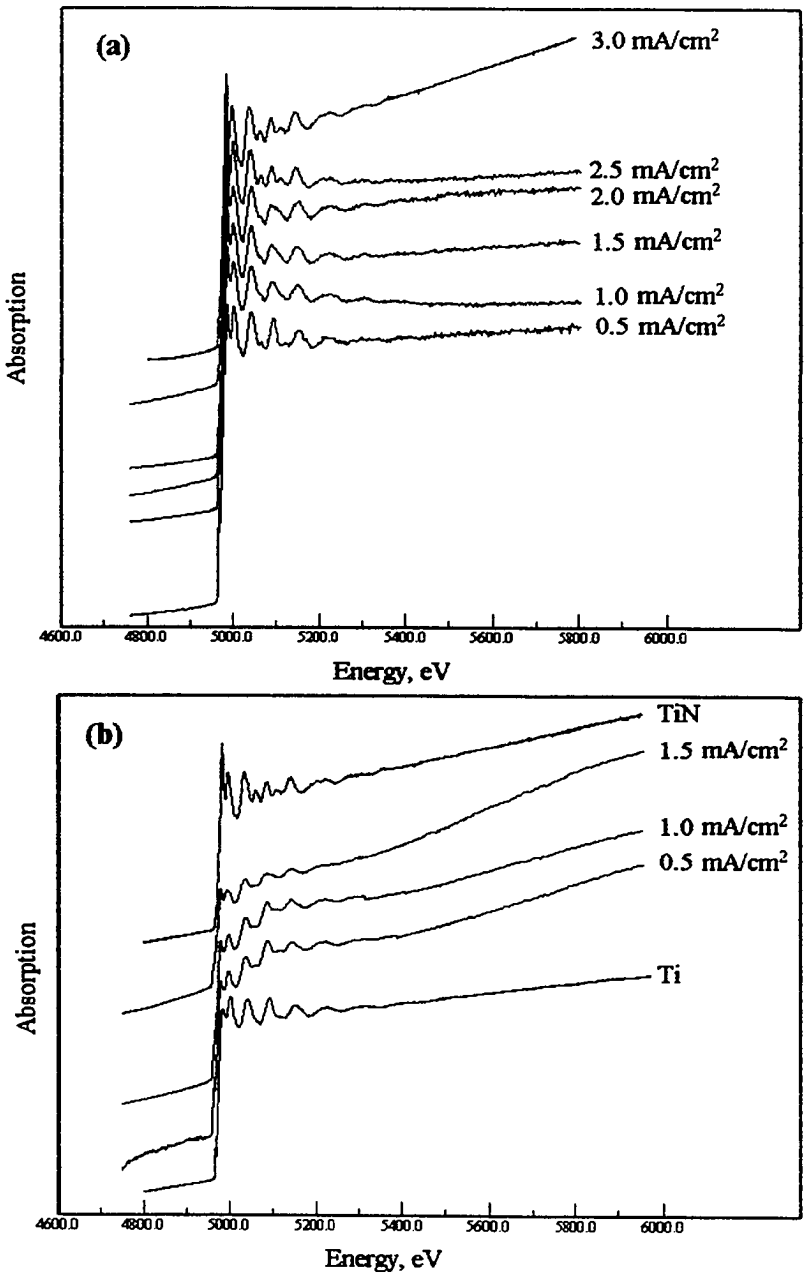

Figure 28 Ti K edge TEY EXAFS raw data of (a) IPAP and (b) conventionally nitrided samples.

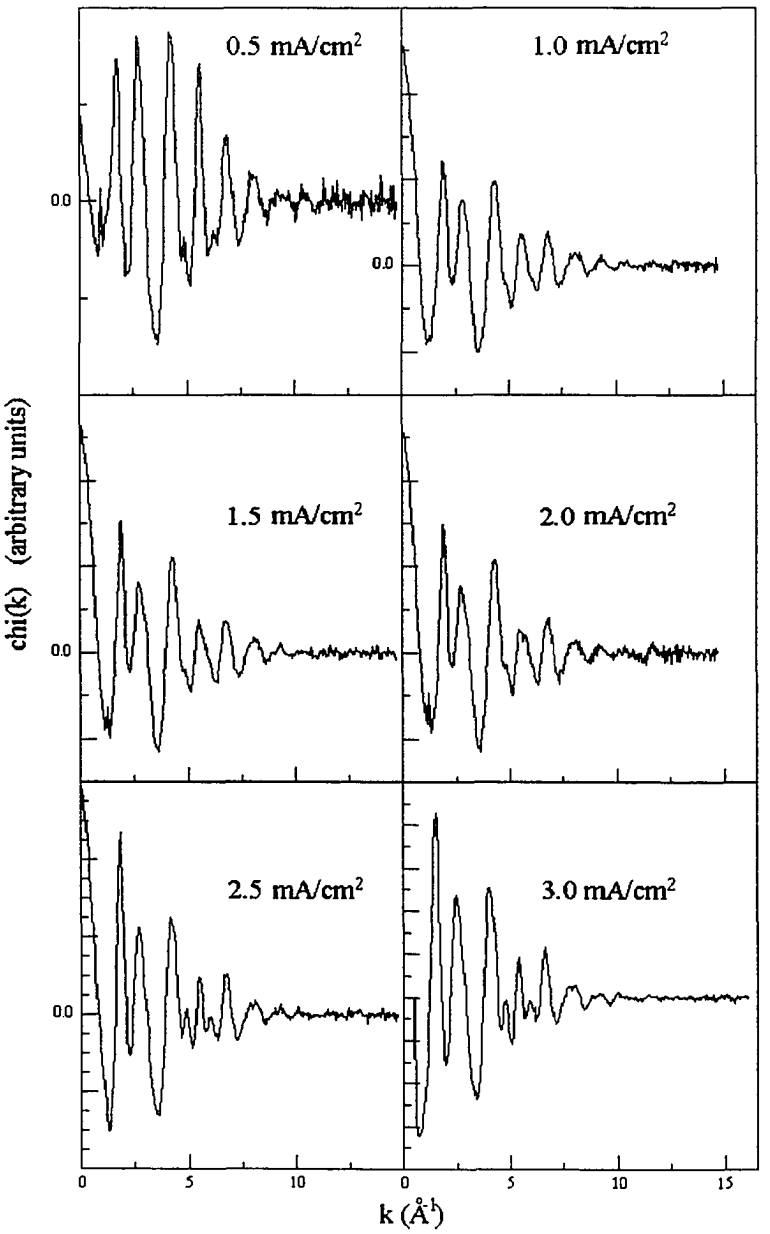

Figure 29 (a)Background removed and normalized Ti K edge TEY EXAFS of IPAP samples.

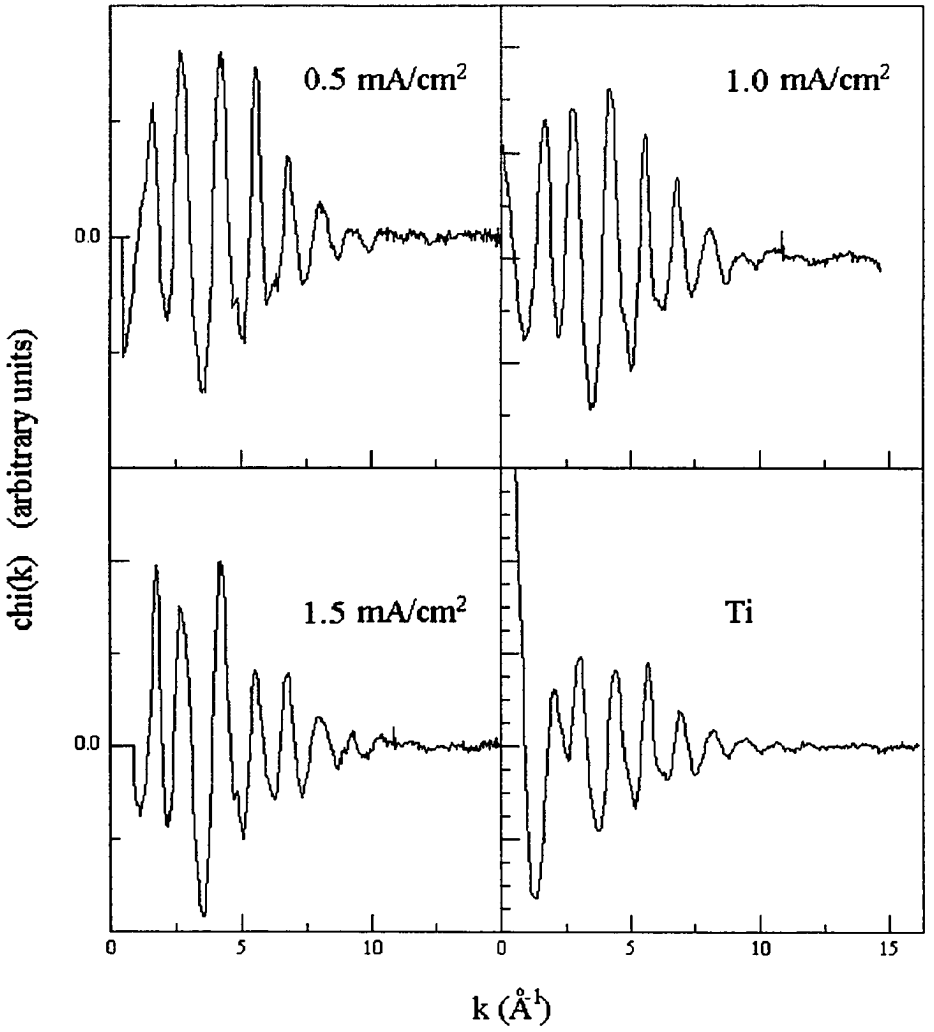

Figure 29 (b)Background removed and normalized Ti K edge TEY EXAFS of conventionally nitrided samples.

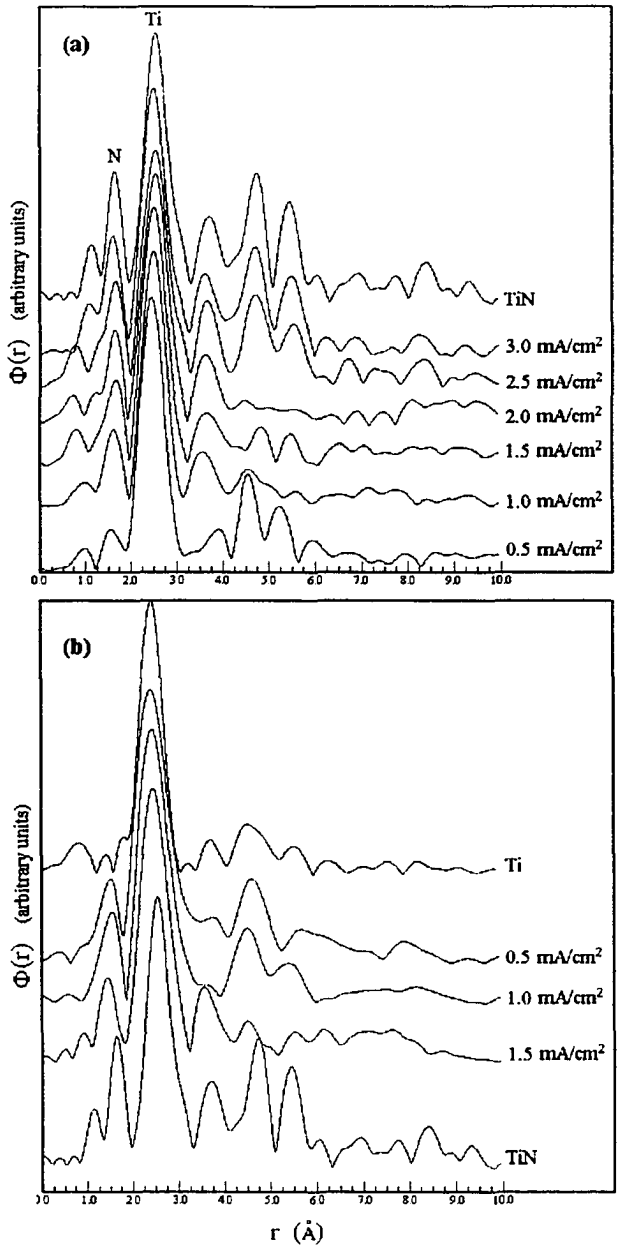

Figure 30 Fourier transforms of Ti K edge TEY EXAFS of TiN, (a) IPAP samples, (b) conventionally nitrided samples.

Table 7 Amplitude ratio of different scattering paths from FEFF calculation.

Path	Amplitude ratio	Degeneracy	nlegs	r effective	Type
1	100.0	6	2	2.1200	SS, 1st shell
2	100.0	12	2	2.9981	SS, 2nd shell
3	13.561	24	3	3.6191	DS
4	35.158	48	3	3.6191	DS
5	31.932	8	2	3.6719	SS, 3rd shell
6	22.012	6	2	4.2400	SS, 4th shell
7	14.021	6	3	4.2400	DS
8	57.778	12	3	4.2400	DS

Since effective path lengths roughly correspond to the peak positions in r space, it is evident that the first coordination shell peak, or scattering path #1, is positioned relatively far from other neighboring paths, such as the second shell peak and the multiple scattering paths. Therefore, it can be assumed that the first peak in r space corresponds to the first coordination shell, and the second peak roughly represents the second shell. In the single scattering case the EXAFS equation can be expressed as

$$\chi(k) = NS_0^2 F(k) e^{-2r/\lambda} e^{-2\sigma^2 k^2} \frac{\sin(2kr + \phi)}{kr^2}. \qquad (19)$$

In this case, the fitted variables are the coordination number N, bond distance r, mean square deviation from the bond distance σ, and the energy shift E_0.

In order to reduce the number of variables in the fit, it was assumed that the path lengths can be expressed as

$$r_i = R_i + \frac{R_i}{R_1} \Delta r_1, \qquad (20)$$

where r_i is the effective path length of the i^{th} path in the fit, R_i is the path length predicted by FEFF, and Δr_1 is the difference between the real and the predicted values

of the first path length. Two Debye-Waller factors, σ_1^2 and σ_2^2, and two shifts of energy origin, ΔE_{01} and ΔE_{02}, for the first and the second shell respectively, were used. Theoretical standards produced by ATOMS and FEFF codes were used in the fit.

The fitting was first performed for the TiN powder sample in order to obtain the amplitude reduction factor S_0^2 by setting the correct coordination numbers and distances. The amplitude reduction factor S_0^2 obtained in the fit is close to the theoretical value of 0.635. The amplitude reduction factor is mostly determined by the central atom and it is transferable between systems with the same central atom. For the k^n weighting function used in Fourier transform, it has been suggested [47] to use n values of 3, 2, and 1 for backscattering atoms with Z<36, 36<Z<57, and Z>57, respectively. For this reason, n=3 has been used in the fits. Quantitative analysis of the local structure was performed by fitting the structural models to the first two coordination shells in the experimental data.

As can be seen from Figure 30, Fourier transforms of the TiN powder and high current density IPAP samples are nearly identical, exhibiting peaks at ~1.75 Å and ~2.70 Å (the Fourier transforms are not phase corrected), which can be assigned to Ti...N and Ti...Ti nearest neighbor interactions at 1.96 Å and 2.99 Å, respectively. Also, the 3.5 Å to 6.0 Å regions of these transforms are very similar, indicating that the longer distance interactions may be equivalent. All other samples exhibit peaks at ~1.75 Å and ~2.70 Å as well, however their 3.5 Å to 6.0 Å regions do not show an obvious match to either Ti metal or TiN, indicating a mixed or intermediate structure. A clear trend can be observed for all samples, with the amplitude of the peak at ~1.75 Å (representing the

Ti...N interaction) gradually increasing with current density. The peak at ~2.70 Å remains at full amplitude in both groups of samples, and can be modeled by a Ti...Ti interaction with a coordination number of 12 in both the Ti and TiN structures. It can be concluded from these observations that the surface structure becomes more like that of pure TiN with increasing current density, which corresponds to an increase in particle energy in IPAP and to an increase in total doze in conventional processing. A similar increase in nearest-neighbor nitrogen with increasing current density is observed for the conventional samples, but the nitrogen peak does not approach the intensity observed in TiN.

Quantitative analysis of the local structure was performed by fitting EXAFS model to the experimental data. Structural parameters, such as coordination numbers (CN) and bond lengths, obtained for all nitrided samples are listed in Table 8. The first shell coordination number in the IPAP processed samples, or the number of nitrogen atoms surrounding a titanium atom, ranged from 5.4 in specimen 6, to only 1.7 in specimen 1. The conventionally nitrided samples showed significant amplitude reduction of the first shell in r space when compared to IPAP samples with the same current densities.

As can be seen from Tables 6 and 8, conventionally processed samples (7-9) demonstrated measurably lower nitrogen coordination numbers than those of IPAP samples prepared at the same current densities, despite a significant increase in the total dose. This is probably due to the fact that average energies of energetic ions and neutrals in these samples are relatively low, 170-211 eV for ions and 81-100 eV for neutrals (Table 6), and the amount of nitriding is determined mainly by the total dose

received by the sample surface. The energy levels in the diode plasma nitriding process do not produce the enhanced diffusion effect in the substrate, such as observed in the IPAP samples. The nitrided layer produced at these conditions is extremely thin, and it is followed by a very narrow diffusion zone, which is in agreement with Auger and electron microscopy results. Moreover, nitrogen CN values are higher for the samples with lower particle energies, thus confirming that for this group of samples the amount of nitrogen in the surface layer is determined primarily by the total dose.

Table 8 Structural parameters obtained from EXAFS simulations for plasma nitrided surfaces.
*Diode plasma nitriding

Sample	n_N	r (Å)	n_{Ti}	r (Å)
1	1.7±0.6	2.073±0.003	11.5±0.6	2.931±0.003
2	3.5±0.8	2.067±0.003	12.1±0.7	2.923±0.003
3	4.0±1.0	2.072±0.005	12.4±0.9	2.930±0.005
4	4.4±1.2	2.070±0.006	12.1±1.2	2.928±0.006
5	5.3±1.0	2.093±0.005	11.6±0.9	2.959±0.005
6	5.4±0.9	2.117±0.004	11.9±0.8	2.994±0.004
7*	0.7±0.5	2.074±0.003	12.0±0.5	2.933±0.003
8*	1.4±0.8	2.069±0.003	11.9±0.7	2.926±0.003
9*	3.3±0.9	2.079±0.004	12.7±0.8	2.941±0.004

IPAP samples (1-6) exhibit significantly increased nitrogen coordination numbers, approaching the stoichiometric value of CN=6 as the current density and the particle energies are increased. IPAP samples demonstrate higher CN values than samples of the second group processed at the same current densities, despite the much lower doses received during processing. This result is also in agreement with Auger and SEM observations. These observations support the previously suggested idea [22] that a certain threshold energy is required for the bombarding particles in order to provide the enhanced diffusion conditions in the surface layer. This requirement was not met in

sample 1, as well as the samples of the second group (6-9), therefore the CN values in these samples are low, and they mainly depend on the total dose received during processing.

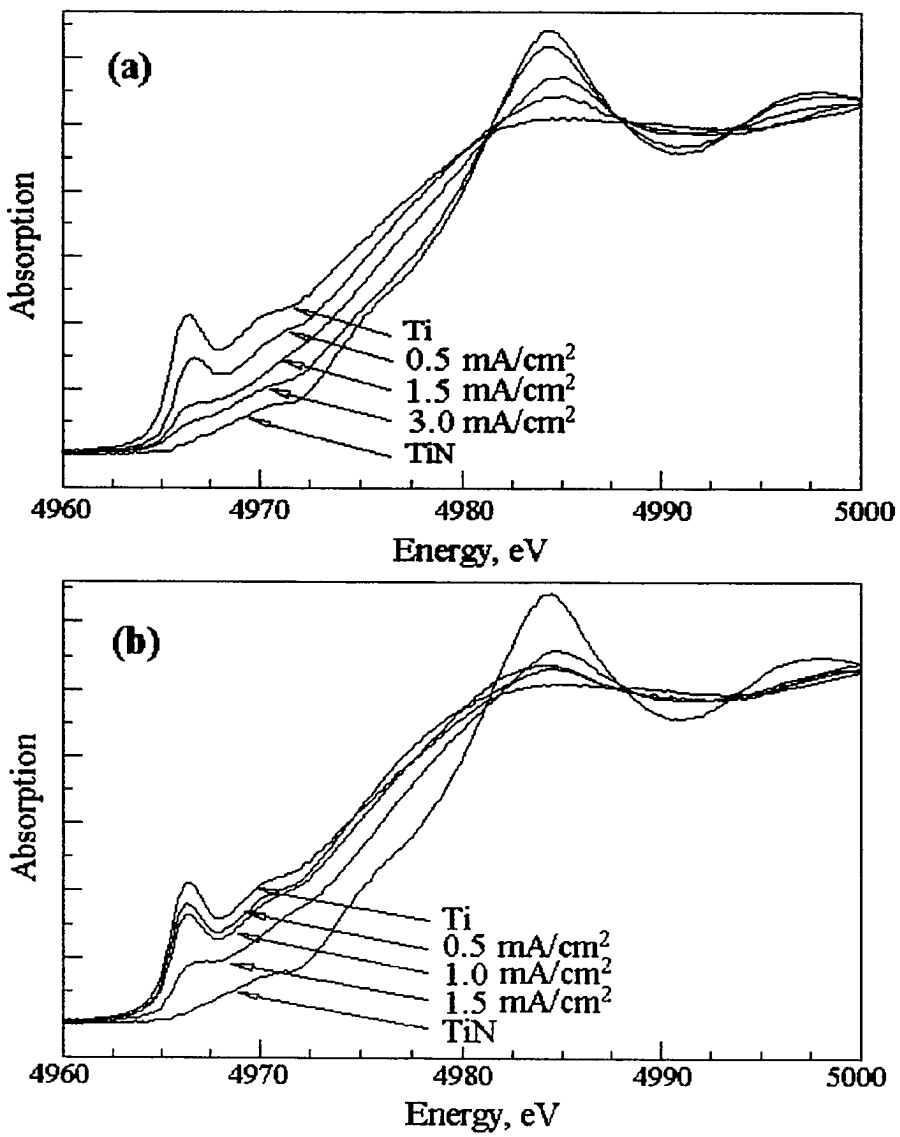

Figure 31 Ti K edge XANES spectra of (a) IPAP and (b) conventionally nitrided samples.

Figure 31 shows normalized spectra of the XANES region for IPAP (a) and conventional (b) samples, shown with the spectra of Ti metal and TiN powder. The Ti metal spectrum exhibits a sharp pre-edge feature at 4966 eV (generally assigned to a $1s \rightarrow 3d$ transition). This pre-edge feature does not appear in the TiN spectrum, which is characterized by a strong "white" line at 4984 eV. In the IPAP samples the trend from a Ti metal-like to a TiN-like spectrum as a function of current density can be followed, with the intensity of the Ti metal pre-edge feature decreasing and the intensity of the TiN white line increasing as current density increases. Sample 1 produced a spectrum which is very similar to that of Ti metal (both in the near edge structure and in the EXAFS region), and sample 6 produced a spectrum which matches well with that of TiN; the intermediate samples appear to be a mixture, with the fraction of TiN signal increasing with the current density. A similar observation can be made for the conventional, or diode glow discharge samples. In this case a point is never reached at which the spectrum closely resembles that of TiN, but again a trend can be observed with the Ti pre-edge feature decreasing and the white line increasing with current density. It is therefore reasonable to attempt to model these spectra as two-phase mixtures of Ti and TiN. Least-squares fitting of the XANES spectra as a linear combination of the spectra of the component phases Ti and TiN was used to obtain quantitative information of the phase fractions. Linear combination XANES fits were performed on the spectra over the region 4950-5000 eV, which covers the Ti metal pre-edge feature and the TiN white line. The results are presented in Table 9 and plotted in Figure 32. For the high energy IPAP samples (5 and 6), very good fits were obtained,

with the system consisting mainly of TiN. Since the two-component model gave good fits to the data, it is taken as a valid model for the surface structure of these samples. For the lower energy IPAP samples and for the conventional samples, less TiN was found in the fits, and the quality of fit factors were not as good. This could be due to the presence of another phase (Ti_2N) or distortion of the α-Ti XANES due to high amounts of interstitial nitrogen. In any case, the fits are a measure of the decrease in the Ti metal pre-edge feature and the corresponding growth of the TiN white line and therefore serve as a good indicator of the overall amount of nitriding.

Table 9 Fraction of δ-TiN phase present at the plasma nitrided surfaces determined by XANES linear combination fitting.

Sample	Current Density, A m^{-2}	%Ti	%TiN	χ^2 10^5
1	5	74.7	25.3	0.63
2	10	56.3	43.77	9.47
3	15	47.8	52.2	3.9
4	20	48.5	51.6	3.3
5	25	21.7	78.3	0.10
6	30	18.1	81.8	0.099
7*	5	86.6	13.55	5.0
8*	10	77.5	22.5	1.6
9*	15	56.18	43.8	3.3

EXAFS analysis was then used to test the two-phase model. This was done by subtracting the Ti metal contributions determined by the XANES analysis (Table 9) from the extracted EXAFS signal. For example, the XANES analysis of the 3.0 mA cm^{-2} IPAP sample (6) indicated the sample to be 18% Ti metal and 82% TiN. The extracted EXAFS signal for the Ti metal standard was therefore multiplied by 0.18, and the result was subtracted from the extracted EXAFS signal for the sample. The resultant EXAFS

spectrum was normalized (multiplied by 1/0.82). EXAFS Fourier transforms of the Ti metal subtracted sample spectra are shown in Figure 33, along with Fourier transforms of TiN and Ti metal. The TiN and sample 6 Fourier transforms are virtually identical, and the Fourier transforms of IPAP samples 3-5 are very similar.

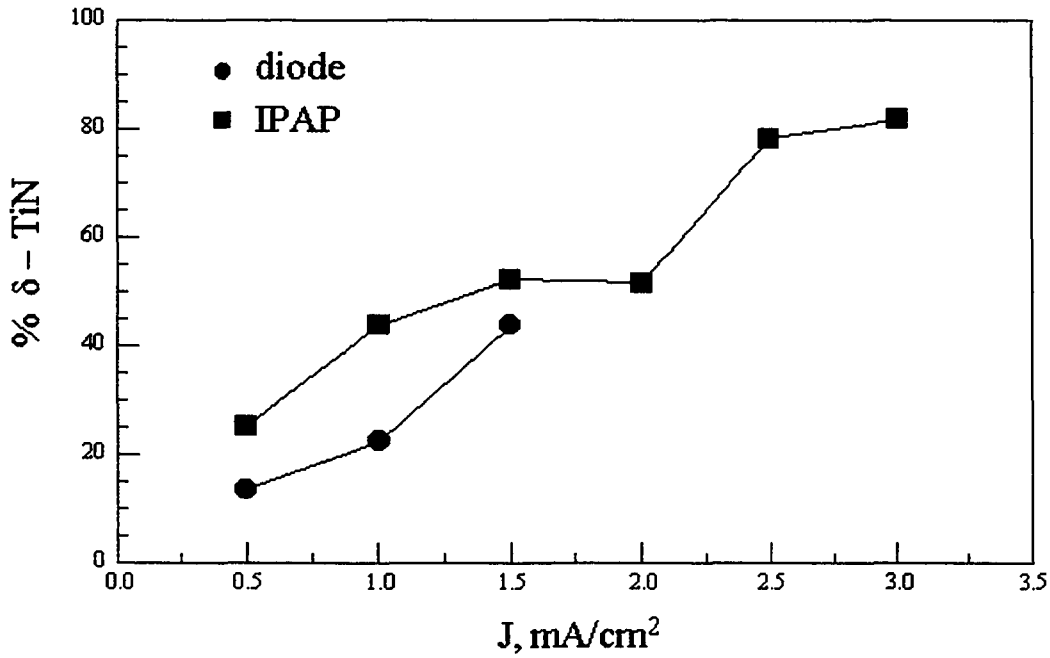

Figure 32 Fraction of δ-TiN phase present at the surface as a function of current density.

Table 10 Structural parameters obtained from EXAFS simulations for plasma nitrided surfaces by using a two-phase model, as discussed in the text.

Sample	n_N	r (Å)	n_{Ti}	r (Å)
1	-	-	-	-
2	6.27±1.1	2.104±0.004	13.9±1.0	2.976±0.004
3	6.39±1.0	2.099±0.004	13.1±0.9	2.968±0.004
4	6.6±1.2	2.099±0.005	12.84±1.1	2.969±0.005
5	5.4±1.0	2.105±0.005	10.7±0.9	2.978±0.005
6	5.8±0.5	2.115±0.002	11.8±0.4	2.992±0.002

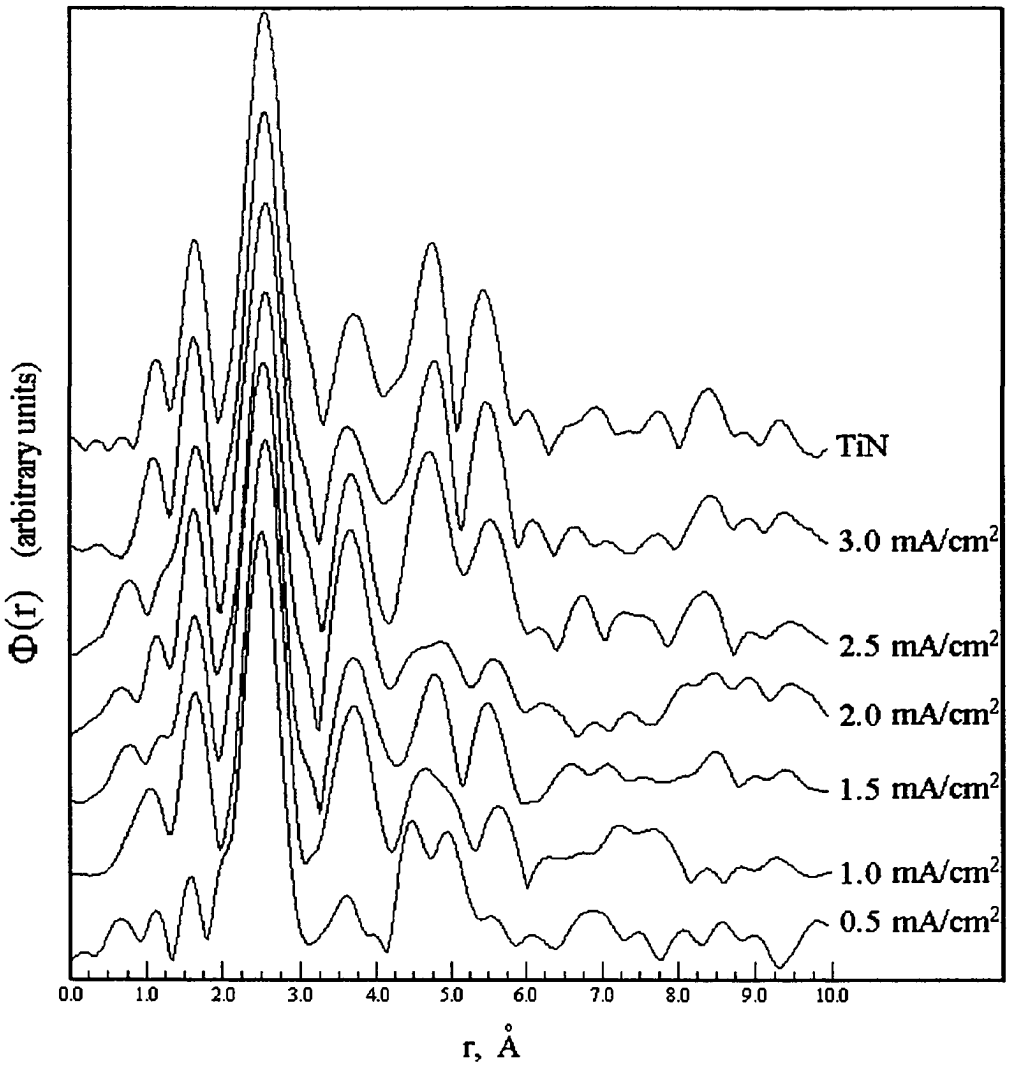

Figure 33 Fourier transforms of EXAFS spectra of IPAP samples obtained for the two-phase surface structure model.

Fitting of the first two shells using FEFF phase and amplitude functions was performed as described above. For sample 6, a good fit was obtained with parameter values very close to those of the TiN standard. The σ^2 values obtained for the TiN powder were used in the fits and it was not necessary to vary them to achieve an acceptable fit. The Ti...N and Ti...Ti coordination numbers are in good agreement with those of stoichiometric TiN, and so are the fit-determined distances. The analysis

indicates the presence of a well ordered stoichiometric TiN phase. The fact that subtracting the Ti metal signal contribution leaves essentially a pure TiN signal strongly supports the two phase model, and it is concluded that the surface structure of sample 6 consists of TiN and a small amount of Ti metal, with other phases present only in minor amounts, if at all. As can be seen in Table 10, similar results were obtained in fitting the 1.0 through 2.5 mA cm^{-2} IPAP samples. For sample 1 the Ti/TiN two phase model breaks down (no good fits based on TiN could be obtained from the Ti metal subtracted EXAFS), suggesting the possible presence of some other phase. Based on the Ti-N phase diagram, the main possibility is the Ti_2N phase, although there is no direct evidence of its presence. Attempts to perform such analysis on the data from the conventional samples were unsuccessful, as in sample 1.

5.2.4 Modeling of produced structures

As can be seen from the Ti-N phase diagram shown in Figure 34 [83], the following phases may exist in the Ti-N system: hexagonal α-Ti, bcc β-Ti, tetragonal ε-Ti_2N, fcc δ-TiN, and its substoichiometric modification δ` which is tetragonally distorted. No changes in the crystal structure of TiN have been reported when nitrogen content exceeds stoichiometry. The α-Ti, ε-Ti_2N and fcc δ-TiN are commonly observed in thin films. The α-Ti phase can dissolve significant amounts (up to 25 at.%) of nitrogen, and the hexagonal lattice is increasingly distorted with N content as nitrogen fills the interstitial sites. Tetragonal ε-Ti_2N phase has been observed both above and below its equilibrium range, in coexistence with δ-TiN and α-Ti phases. So far, all

attempts to synthesize films consisting entirely of Ti_2N have been unsuccessful, which can be explained by the extremely narrow equilibrium range of this phase.

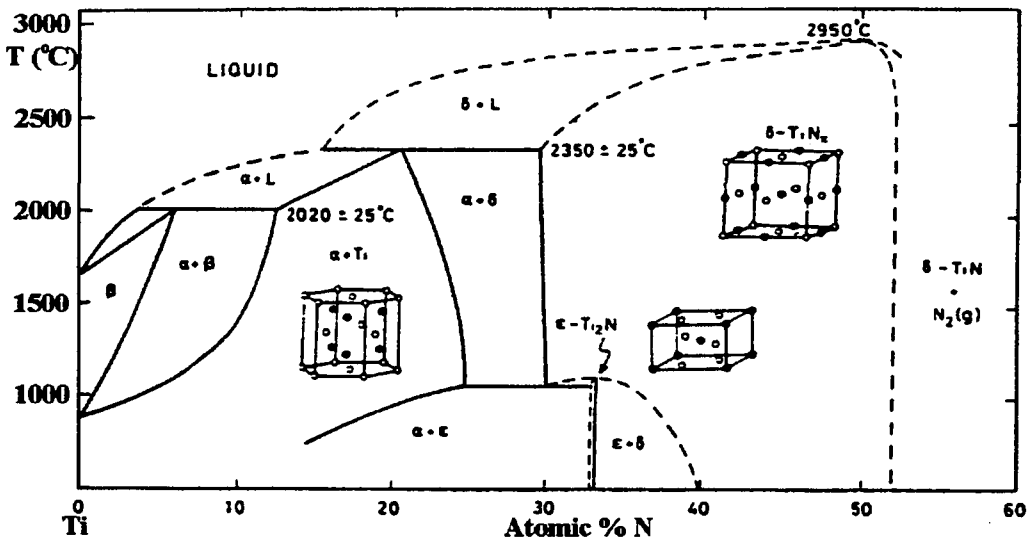

Figure 34 Phase diagram of the Ti-N system [83].

Asplund et al. [84] reported a mixed ε-Ti_2N and δ-TiN structure, with metastable α-Ti present up to about 50 at.% N. In their study, both α-Ti and ε-Ti_2N in nitrogen-rich films were transformed into δ-TiN after annealing at 900 °C for 2 hours. In an x-ray diffraction study of Ti-N films produced by triode ion plating [85], the ε-Ti_2N was observed at about 30 at.% N, and the δ-TiN appeared above 33 at.% N.

In the Ti-N system, nitrogen first occupies octahedral interstices, causing the lattice parameter to increase. Nitrogen occupation of interstitial sites locks diffusion paths and thus stabilizes the structure. The δ-TiN phase is also known as an efficient diffusion barrier [83]. Therefore, successful nitriding of titanium at low temperatures requires an effective diffusion-enhancement mechanism, such as energetic particle bombardment.

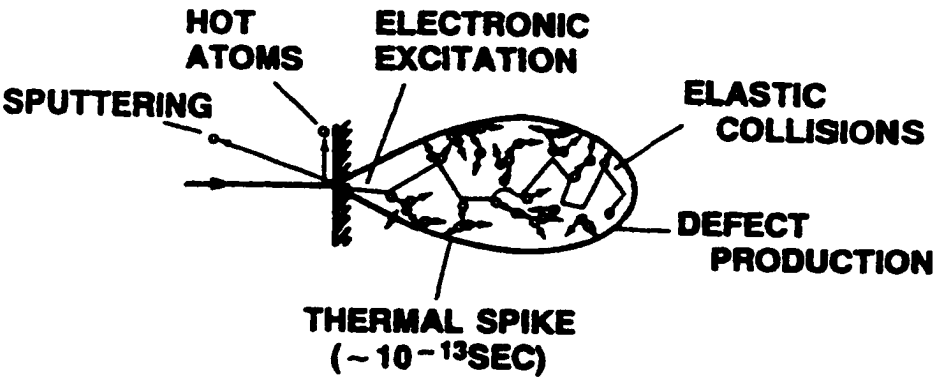

Figure 35 Processes in collision cascade produced by impact of energetic ion with solid [86].

The processes by which energy is transferred from an energetic ion to a solid are fundamental for understanding how energetic particle bombardment interacts with a material to modify its microstructure and properties. Various effects resulting from the impact of an energetic ion with a solid are illustrated schematically in Figure 35 [86]. The incoming ion loses energy by inelastic collisions which produce electronic excitations, and by elastic collisions which displace target atoms from their lattice positions. The displaced atoms produce additional collisions over a short period of time, and the resulting series of events is called a collision cascade [86]. Each atom continues to undergo collisions until the energy drops below the level needed to displace an atom from its lattice position (~ 25 eV).

The energy of the bombarding particle is a critical parameter, especially in the low energy regime, because some processes such as dissociation, desorption, and defect production have a threshold below which the process does not occur.

At low energies, cascades occur near the surface, resulting in sputtering of the surface atoms and desorption of adsorbed species. At higher energies, the penetration

depth of the incoming ions is increased, producing more "bulk" rather than "surface" defects, thus increasing the diffusion rate. Recent TRIM calculations [44] showed that the average implantation depth for nitrogen ions at 200 eV is approximately 10 Å, with 3 vacancies generated by each ion. At the energies of 1000 - 1100 eV the implantation depth increased to approximately 30 Å, and the number of vacancies generated per ion was reported as 15 - 18. These findings are consistent with our experimental results, where in the diode-processed samples the nitrogen concentration was found to be very high at the surface (~50 at. %), but rapidly decreased with depth, reaching almost zero at 500 nm (Fig. 27). In this low-energy/high-doze regime, the sample surface may become saturated with nitrogen at the initial stages of the nitriding process. As discussed above, formation of saturated solid solution of nitrogen in α-Ti and titanium nitride phases will block the diffusion of nitrogen into the substrate, resulting in very shallow nitrided layers. Thus, the energy levels achieved in the diode process (200 eV and below) are insufficient to produce the enhanced diffusion effect. The average ion energy used in IPAP plasma nitriding in this work ranged from approximately 600 to 1100 eV, resulting in much deeper nitrided layers and higher δ-TiN fractions than those achieved by diode processing at the same current densities. Therefore, it seems likely that the threshold energy needed to produce enhanced nitrogen diffusion lies between 200 and 600 eV, in agreement with the previously reported theoretical value of 440 eV [44].

Another way of viewing the ion-solid interaction is as an energy deposition process, as proposed by Seitz and Koehler [87]. They suggested the concept of thermal

spikes, where the temperature in a localized region could approach or even exceed the melting point of the solid as a result of the localized energy deposition in the cascade.

Molecular dynamics simulations of energetic (3 and 5 keV) collision cascades in copper reported recently by Averback et al. [88] demonstrated that the temperature in the cascade region exceeded the melting point of copper and thus the central region of the cascade undergoes melting. It is, therefore, possible that as the energy of the bombarding ions utilized in plasma nitriding approaches a certain threshold value, thermal spikes produced in the collision cascades become an important factor. As can be seen from Figure 34, formation of the ε-Ti_2N phase will be suppressed in the areas where the temperature exceeds ~1000 °C, since only α-Ti and δ-TiN are the thermodynamically stable phases in that region. Although the equilibrium phase diagram is not directly applicable to a highly non-equilibrium process such as energetic ion bombardment, we suggest that the stable phases existing in the Ti-N system play an important role in the formation of the surface structure. Therefore, based on the experimental results we suggest that temperatures in excess of 1000 °C may be generated in the collision cascades as the average ion energy reaches approximately 1 keV, creating conditions that favor the formation of a mostly two-phase structure (α-Ti and δ-TiN). Another important factor that has to be considered is the relatively high current density (2.5 - 3.0 mA cm^{-2}) corresponding to this energy range. This translates into a greater number of ion collisions per unit area per unit time, and may allow this proposed mechanism to create a very thin (2 - 3 nm), continuous surface layer

consisting primarily of TiN with small amount of α-Ti nitrogen solid solution present, as seen from the EXAFS and XANES measurements.

CHAPTER 6

SUMMARY

Diamondlike films studied in the present work included DLC films deposited on various substrates in the presence of a Si bond layer by using ionized CH_4, and Si-containing DLC films on Si substrates produced by ion (Ar^+) beam assisted deposition. These films were found to be featureless, very smooth, dense and of high hardness. Auger spectra and electron diffraction patterns demonstrated mostly amorphous nature of the films. For the Si-free DLC films, IR spectroscopy revealed the presence of both sp^3 and sp^2 carbon-bonded hydrogen in the films, with a ratio ranging approximately between 3.2 and 4.1. The ratio of the diamondlike to graphitelike carbon in the films obtained by Raman spectroscopy varied approximately between 1.8 and 2.6. The relatively lower ratio obtained by Raman spectroscopy as compared to the IR results may be attributed to D line contributions to the diamondlike phase band of the Raman spectrum. An observation was made that DLC films deposited on ion-beam assisted Si interlayers exhibited more diamondlike character. This effect can be attributed to the higher surface roughness of the Si interlayer produced under the energetic bombardment. Based on these findings, a microstructure that can be described as small graphitelike clusters interconnected by a network of sp^3-bonded carbon is suggested.

Characterization of the Si-DLC films by IR spectroscopy demonstrated a wide variation in the sp^3/sp^2 ratio, ranging between 1.5 and 5.4. As demonstrated by the IR

results, Si atoms participate in the DLC structure by tetrahedral bonding with hydrogen and CH_n groups. Incorporation of Si in DLC structure seems to prevent the formation of aromatic structures, usually observed in DLC films, and to promote the formation of sp^3 bonds, producing much higher sp^3/sp^2 ratio under certain conditions than previously observed for DLC films [11]. The effect of energetic ion bombardment was investigated, resulting in the conclusion that low current density conditions apparently favor the participation of Si in tetrahedral Si-C bonds, producing more diamond-like behavior and increased hardness, while increased current density promotes the formation of Si-H bonds and results in softer coatings. Based on these experimental results, a different structural model is suggested for the Si-DLC films, which consists of an sp^2-sp^3 carbon network with the $C(sp^2)$ atoms present in olefinic rather than aromatic bonding units. This network is composed of two fundamental structural units, $C(sp^3)$-centered tetrahedral and $C(sp^2)$=$C(sp^2)$-centered planar bonding units.

Two sets of Ti specimens have been processed in the course of this work, by using glow discharge triode (IPAP) and diode plasma nitriding. Their characterization was performed by TEY EXAFS and XANES, SEM, and AES.

The effect of the using the IPAP intensified glow discharge system on the thickness of the nitrided layer can be seen from the SEM and AES results. Using the conventional diode ion nitriding system produces only a very thin nitride (TiN and Ti_2N) surface layer. In contrast, for the IPAP samples, the thickness of this layer was estimated from the SEM results as approximately 3-5 μm. This may be accomplished

through enhanced diffusion caused by the creation of defects and local heating from the impact of the relatively high energy particles in the IPAP process.

EXAFS and XANES examination demonstrated that nitrogen present in the modified layer produced by IPAP can be successfully detected and studied by x-ray absorption techniques. First, quantitative analysis of the local structure were performed by fitting a one-phase δ-TiN model to the experimental EXAFS data. The fitting results demonstrated that the nearest-neighbor N coordination number increases and the fit quality improves with increasing current density. It was shown that varying amounts of FCC-coordinated TiN structure were produced at the sample surface, depending on the deposition parameters. Processing conditions corresponding to the highest energies of the bombarding particles ($E \geq 1$ keV) that were achieved in IPAP samples resulted in the outer layer structure virtually identical to that of the pure TiN standard. A decrease in the average particle energy leads to diminishing amounts of the stoichiometric TiN phase produced in the surface layer, as illustrated by both EXAFS and XANES analysis. Based on these findings, a two-phase model of the outer layer was proposed and quantitatively tested by fitting to the experimental EXAFS data. This model, describing the outer layer structure as a mixture of δ-TiN and α-Ti, was found to be in good agreement with experimental data only for IPAP samples processed at the highest particle energies, with E_I^a approaching 1 keV and above. At lower particle energies, however, this two-phase model fails to describe the structure of the nitrided layer, possibly due to increasing amounts of the third phase known to exist in the Ti-N system, ε-Ti_2N.

The combined results of SEM, AES, and XAFS therefore give a good characterization of the system, with a thin nitrided layer consisting of mainly TiN at the surface, followed by Ti_2N and α-Ti. To produce such a surface with ion nitriding, it was necessary to use IPAP nitriding at high current densities (and therefore high particle energies). Using the IPAP method at lower current densities produced a relatively thick nitrided layer, but did not produce a well-formed TiN phase at the surface. Ion nitriding with the conventional diode system produced only a very thin nitrided layer (<500 nm) and failed to produce a good TiN surface layer.

The results of this study are expected to improve our understanding of the structure of titanium nitride produced by IPAP, its relationship with processing parameters, and the mechanism of enhanced plasma ion nitriding.

REFERENCES

[1] S. Aisenberg and R. Chabot, *J. Appl. Phys.*, 42, (1971) 2953.

[2] H. Tsai and D. B. Bogy, *J. Vac. Sci. Technol. A* 5, (1987) 3287.

[3] S. Matsumoto, Y. Sato, M. Tsutsumi and N. Setaka, *J.Mater. Sci.*, 17, (1982) 3106.

[4] D.P. Dowling et. al., *Surface and Coatings Technology*, 53 (1992) 177.

[5] J. Robertson, *Prog. Solid St. Chem.*, 21, (1991) 199.

[6] F.M. Kimock and B.J. Knapp, *Surface and Coatings Technology*, 56, (1993) 273.

[7] M. A. Tamor, C. H. Wu, *J. Appl. Phys.*, 67 (1990) 1007.

[8] N.A.Marks et. al., *Phys. Rev. Letters*, 76 (1996) 768.

[9] C.Z. Wang et.al., *Phys.Rev.Lett.*, 70, (1993) 611.

[10] G. Comelli, J. Stohr, C.J. Robinson, and W. Jark, *Phys. Rev.* B, 38, (1988) 7511.

[11] J. Robertson and E.P. O'Reilly, *Phys. Rev.* B , 35 (1987) 2946.

[12] C. Jaeger et.al., *Phys.Rev.*, B 50, (1994) 846.

[13] V. Palshin, S. Ves, S. Logothetidis and E. I. Meletis, *Thin Solid Films*, 270 (1995) 165.

[14] X. He, W. Li and H. Li, *J. Vac. Sci. Technol.A*, A11 (1993) 2964.

[15] E. J. Spenser, P. H. Schmidt, D. C. Joy and F. J. Sausalone, *Appl. Phys. Lett.*, 129 (1976) 118.

[16] T. Mori and Y. Namba, *J. Vac. Sci. Technol. A*, A1 (1983) 23.

[17] C. C. Chang, *J. Vac. Sci. Technol.*, 18 (1981) 276.

[18] S. Berg and L. P. Andersson, *Thin Solid Films*, 58 (1979) 117.

[19] M. J. Mirtich, D. M. Swec and J. C. Angus, *Thin Solid films*, 131 (1985) 245.

[20] J.W. Zou, K. Schmidt, K. Reichelt and B. Dischler, *J. Appl. Phys.*, 67 (1990) 487.

[21] B. Dischler, G. Brandt and P. Koidl, *Appl. Phys. Lett.*, 42 (1983) 636.

[22] J. Xu and E.I. Meletis, in J. Singh and S.M. Copley (eds.) *Beam Processing of Advanced Materials*, The Metallurgical Society, Warrendale, PA, (1993), 551.

[23] E.I. Meletis and S. Yan, *J. Vac. Sci. Technol.*, 11 (1) (1993) 25.

[24] T.M. Muraleedharan and E.I. Meletis, *Thin Solid Films*, 221 (1992) 104.

[25] E.I. Meletis and S. Yan, *J. Vac. Sci. Technol.*, 9 (4) (1991) 2279.

[26] A.Adjaottor, E. Ma and E.I. Meletis, *Elevated Temperature Coatings: Science and Technology I*, N.B. Dahotre, J.M. Hampikian and J.J. Stilich eds., TMS-AIME, Warrendale, PA, (1995).

[27] J. Xu, *The Role of Energetic Particle Bombardment in Enhanced Glow Discharge Ion Nitriding*, MS Thesis, Louisiana State University, (1993).

[28] A. Leyland, K.S. Fancey and A. Matthews, *Surf. Eng.*, 7 (3) (1991) 207.

[29] A. Matthews and D.G. Teer, *Thin Solid Films*, 80 (1981) 41.

[30] *Ion Nitriding*, Ed. E T. Spalvins, ASM, Materials Park, OH, (1987).

[31] *Surface Modification Technologies IX*, Ed. T.S. Sudarshan TMS-AIME, Warrendale, PA, (1996).

[32] B.N. Chapman, *Glow Discharge Processes*, John Wiley and Sons, New York, (1980).

[33] K.S. Fancey and A. Matthews, *Surf. Coat. Technol.*, 33 (1987) 17.

[34] J. Rickards, *Vacuum*, 34 (5) (1984) 559.

[35] A.V. Seybolt, *Met. Prog.*, 245 (1969) 769.

[36] G. Tibbetts, *J. Appl. Phys.*, 45 (1974) 5072.

[37] J.A. Taylor, G.M. Lanchester, A. Ignatien and J.W. Rabalais, *J. Chem. Phys.*, 68 (1978) 1776.

[38] H.D. Hangstrum, *Phys. Rev.*, 123 (1961) 758.

[39] J. Michalski, *Surf. Coat. Technol.*, 59 (1993) 321.

[40] H. Hudis, *J. Appl. Phys.*, 44 (1973) 1489.

[41] W. Shockley, *Dislocations and Mechanical Properties of Crystals*, John Wiley & Sons, New York, (1957) 581.

[42] C.K. Jones and S.W. Martin, *Met. Prog.*, 85 (1964) 95.

[43] A. Brokman and F.R. Tuler, *J. Appl. Phys.* 52 (1) (1981) 468.

[44] A. Adjaottor, *A Study of the effect of Energetic Flux Bombardment on Intensified Plasma-Assisted Processing*, Ph.D. dissertation, Louisiana State University, (1997).

[45] J.F. Ziegler, J.P. Biersack and U. Littmark, *The Stopping and Range of Ions in Solids*, Pergamon Press, New York, (1985).

[46] D.C. Koningsberger and R.Prins, *X-Ray Absorption: Principles, Applications, Techniques of EXAFS, SEXAFS, and XANES*, John Wiley & Sons, (1988).

[47] B.K. Teo, *EXAFS: Basic Principles and Data Analysis*, Springer-Verlag, Berlin, Heidelberg, New York, Tokyo, (1986).

[48] C.G. Fountzoulas et.al., *Mater. Res. Soc. Proc. Symp.* 279, (1992) 645.

[49] C.G. Fountzoulas, T.Z. Kattamis and M. Chen, *Mater. Res. Soc. Proc. Symp.* 316, (1994) 851.

[50] C.G. Fountzoulas et.al., *J. Vac. Sci. Technol.*, B 12(2), (1994) 977.

[51] P.J. Schilling et.al., *Rev. Sci. Instrum.*, 66, (1994) 2214.

[52] E.I. Meletis, A. Erdemir and G. Fenske, *Surf. Coat. Technol.*, 73 (1995) 39.

[53] T.J. Moravec and T.W Orent, *J. Vac. Sci. Technol.*, 18 (1981) 226.

[54] D.A. Anderson, *Phil. Mag.*, 35 (1977) 17.

[55] L.C. Nistor, J. Van Landuyt, V.G. Ralchenko, T.V. Kononenko, E.D. Obraztsova and V.E. Strelnitsky, *J. Appl. Phys. A*, 58 (1994) 137.

[56] A.H. White and L.H. Germer, *J. Chem. Phys.*, 9 (1941) 492.

[57] J. Kakinoki, K. Katada, T. Hanawa and T. Ino, *Acta Crystallogr.*, 13 (1960) 171.

[58] A. Oberlin, M. Oberlin and M. Maubois, *Phil. Mag.*, 32 (1975) 833.

[59] W. Zhu, C.A. Randall, A.R. Badzian and R. Messier, *J. Vac. Sci. Technol. A*, 7 (1989) 2315.

[60] J. Robertson, *Advan. Phys.*, 35 (1986) 317.

[61] C.V. Cooper, C.P. Beetz, Jr., B.W. Buchholtz, P.J. Wilbur and R. Wei, *Diamond Relat. Mater.*, 3 (1994) 534.

[62] D. Beeman, J. Silverman, R. Lynds and M.R. Anderson, *Phys Rev.*, B30 (1984) 870.

[63] A. Richter, H.J. Scheibe W. Pompe, K.W. Brzezinka and I. Muhling, *J. Non-Cry. Solids*, 88 (1986)1 31.

[64] W.S. Baska, J.S. Lannin, D.L. Pappas and J.J. Cuomo, *Phys. Rev.*, B47 (1993) 10931.

[65] M. Yoshikawa, G. Katargiri, H. Ishida, A. Ishitani and T. Akamatsu, *Sol. State Commun.*, 66 (1988) 1177.

[66] R.O. Dillon, J. Woollam and V. Katkanant, *Phys. Rev.*, B29 (1984) 3482.

[67] J. Wagner, M. Ramsteiner, Ch. Wild and P. Koidl, *Phys. Rev.*, B40 (1989) 1817.

[68] M. Ramsteiner and J. Wagner, *Appl. Phys. Lett.*, 51 (1987) 1355.

[69] F. Tuinstra and J.L. Koening, *J. Compos. Mater.*, 4 (1970) 492.

[70] B. Dischler, A. Bubenzer and P. Koidl, Solid State Commun., 48 (1983) 105.

[71] Y. Liu , A. Erdemir and E.I. Meletis, *Surface and Coatings Technology*, 82 (1996) 48-56.

[72] Y. Liu, A. Erdemir and E.I. Meletis, *Surface and Coatings Technology*, 86-87 (1996) 564-568.

[73] Y. Liu, A. Erdemir and E.I. Meletis, *Surface and Coatings Technology*, 94-95 (1997) 463-468.

[74] Y. Liu and E.I. Meletis, *Journal of Materials Science*, 32 (1997) 3491-95.

[75] J. Bullot and M.P. Schmidt, *Phys. Stat. Sol.* (b), 143 (1987) 345.

[76] B. Dischler, *Europian Materials Research Society Symposia Proceedings (Strasbourg)*, 17 (1987) 189.

[77] Pouchert, Charles J., *The Aldrich library of infrared spectra*, Aldrich Chemical Co., Milwaukee, Wisconsin, (1981).

[78] Nakamoto, Kazuo, *Infrared spectra of inorganic and coordination compounds*, Wiley-Interscience, New York, (1970).

[79] M.N.P. Carreno and I. Pereyra, *Journal of Applied Physics*, 75 (1) (1994) 538.

[80] W. Moller, *Appl. Phys. Lett.* 59 (1991) 19.

[81] Z.L. Akkerman, H. Efstathiadis, and F.W. Smith, *J.Appl.Phys.*, 80, (1996) 3068.

[82] H. Efstathiadis, Z.L. Akkerman, and F.W. Smith, *J.Appl.Phys.*, 79, (1996) 2954.

[83] J.M. Molarius, A.S. Korhonen, and E.O. Ristolainen, *J. Vac. Sci. Technol.*, A 3 (6), (1985) 2419

[84] M. Asplund, A.S. Korhonen, J.M. Molarius, E. Nykanen, and M.S. Sulonen, *Mat. Res. Soc. Symp.Proc.*, 54, (1986) 541.

[85] J.M. Molarius, A.S. Korhonen, E. Erola, and E. Nykanen, *Mat. Res. Soc. Symp.Proc.*, 68, (1986).

[86] F.A. Smidt, *International Materials Reviews*, 35 (1990) 61.

[87] F. Seitz and J.S. Koehler, *Solid State Phys.*, 2 (1956) 307.

[88] R.S. Averback, T. Diaz de la Rubia, H. Hsieh and R. Benedek, *Nucl. Instrum. Meth. Phys. Res.*, B59/60 (1991) 709.

VITA

Vadim Palshin was born on July 25, 1969, in Nikolaev, Ukraine. In 1986, he left for Moscow, Russia, to study in Moscow Institute of Physics and Technology. In 1990, he returned to Kiev to complete his last two years of study at the Kiev Branch of Moscow Institute of Physics and Technology, and graduated with a Bachelor of Science in Applied Physics and Mathematics in 1992.

In 1993 he began graduate work in the Department of Engineering Science at Louisiana State University in Baton Rouge, Louisiana. He is currently a candidate for the degree of Doctor of Philosophy in Engineering Science to be awarded at the Summer commencement, 1998.

DOCTORAL EXAMINATION AND DISSERTATION REPORT

Candidate: Vadim G. Palshin

Major Field: Engineering Science

Title of Dissertation: CHARACTERIZATION AND MODELING OF ADVANCED MODIFIED SURFACES

Approved:

Major Professor and Chairman

Dean of the Graduate School

EXAMINING COMMITTEE:

Date of Examination:

07/13/ 98

IMAGE EVALUATION TEST TARGET (QA-3)

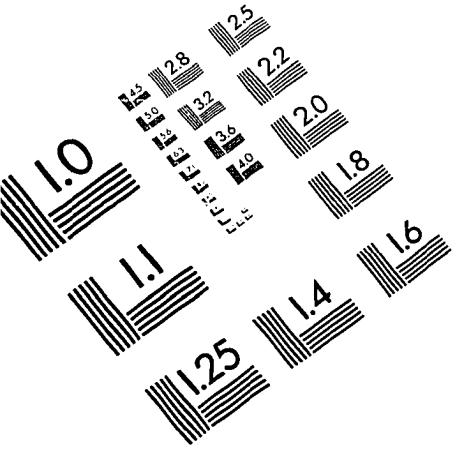

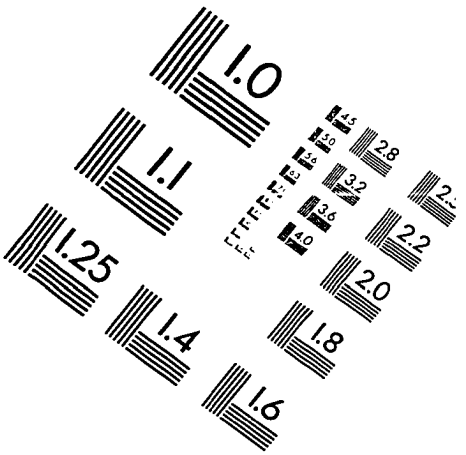

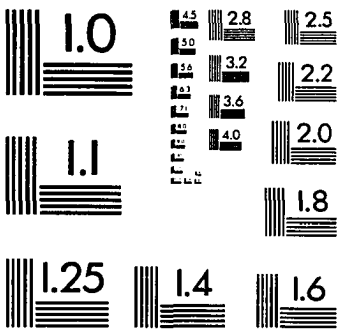

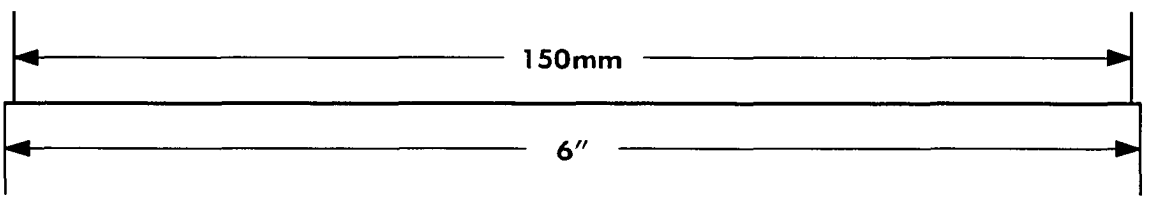

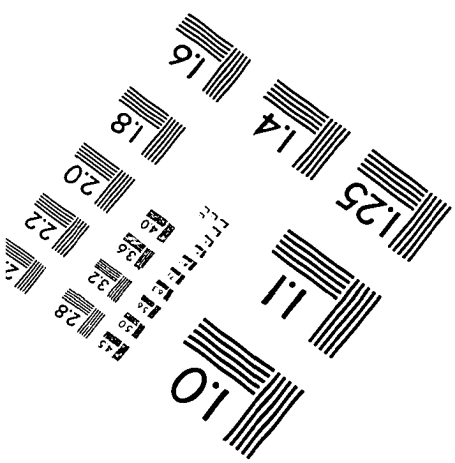

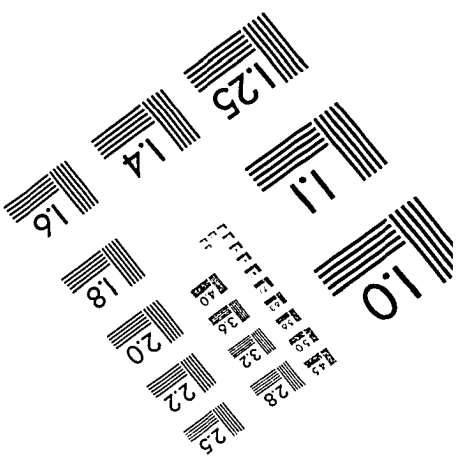

APPLIED IMAGE, Inc
1653 East Main Street
Rochester, NY 14609 USA
Phone: 716/482-0300
Fax: 716/288-5989